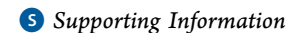
# **Inorganic Chemistry**

# Redox-Active Bis(phenolate) N-Heterocyclic Carbene [OCO] Pincer Ligands Support Cobalt Electron Transfer Series Spanning Four Oxidation States

Caleb F. Harris, \*\bigodom Michael B. Bayless, \*\text{ Nicolaas P. van Leest, \*\text{ Quinton J. Bruch, \*\text{ Brooke N. Livesay, \* John Bacsa, \*\text{ In Matthew P. Shores, \*\text{ \in 0} Bas de Bruin, \*\text{ \in 0} and Jake D. Soper \*\text{ \in 0} }

X-ray Crystallography Center, Department of Chemistry, Emory University, 1515 Dickey Drive, Atlanta, Georgia 30322, United States



ABSTRACT: A new family of low-coordinate Co complexes supported by three redox-noninnocent tridentate [OCO] pincertype bis(phenolate) N-heterocyclic carbene (NHC) ligands are described. Combined experimental and computational data suggest that the charge-neutral four-coordinate complexes are best formulated as Co(II) centers bound to closed-shell [OCO]<sup>2-</sup> dianions, of the general formula [(OCO)Co<sup>II</sup>L] (where L is a solvent-derived MeCN or THF). Cyclic voltammograms of the [(OCO)Co<sup>II</sup>L] complexes reveal three oxidations accessible at potentials below 1.2 V vs Fc<sup>+</sup>/Fc, corresponding to generation of formally Co(V) species, but the true physical/spectroscopic oxidation states are much lower. Chemical oxidations afford the



mono- and dications of the imidazoline NHC-derived complex, which were examined by computational and magnetic and spectroscopic methods, including single-crystal X-ray diffraction. The metal and ligand oxidation states of the monocationic complex are ambiguous; data are consistent with formulation as either [(SOCO)Co<sup>III</sup>(THF)<sub>2</sub>]<sup>+</sup> containing a closed-shell  $[^{S}OCO]^{2-}$  diphenolate ligand bound to a S=1 Co(III) center, or  $[(^{S}OCO^{\bullet})Co^{II}(THF)_{2}]^{+}$  with a low-spin Co(II) ion ferromagnetically coupled to monoanionic [SOCO•] containing a single unpaired electron distributed across the [OCO] framework. The dication is best described as [(SOCO0)CoII(THF)3]2+, with a single unpaired electron localized on the d7 Co(II) center and a doubly oxidized, charge-neutral, closed-shell SOCO ligand. The combined data provide for the first time unequivocal and structural evidence for [OCO] ligand redox activity. Notably, varying the degree of unsaturation in the NHC backbone shifts the ligand-based oxidation potentials by up to 400 mV. The possible chemical origins of this unexpected shift, along with the potential utility of the [OCO] pincer ligands for base-metal-mediated organometallic coupling catalysis, are discussed.

### INTRODUCTION

Cost, toxicity, and sustainability concerns motivate the continued pursuit of base metals as alternatives to preciousmetal catalysts for small-molecule and fine-chemical transformations, including hydrogenation, C-C and C-X crosscoupling, and C-H bond functionalization protocols. 1-3 The utility of platinum-group metals for such processes derives from their capacity to mediate the multielectron organometallic bond-making and -breaking steps which comprise most catalytic cycles. 4,5 Selectivity in these systems is therefore a consequence of their thermodynamic bias for concerted twoelectron transfer. 4,6 Accordingly, efforts to develop base-metal alternatives must address the propensity of later 3d metals to exist in oxidation states that differ by only one electron.

One potential solution is to expand the redox sphere beyond the metal center by harnessing cooperative metal-ligand redox processes for multielectron chemistry. 3,8-12 In this approach, the capacity of redox-active ligands to store and deliver charge is a tool to bring about precious metal-like two-electron organometallic reactivity at metal ions that are more commonly prone to one-electron transfer or that are even redox inert. This strategy has recently been applied to a wide array of bond-

Received: July 26, 2017 Published: October 2, 2017

<sup>&</sup>lt;sup>†</sup>School of Chemistry and Biochemistry, Georgia Institute of Technology, Atlanta, Georgia 30332-0400, United States

<sup>&</sup>lt;sup>‡</sup>Van 't Hoff Institute for Molecular Sciences (HIMS), University of Amsterdam (UvA), Science Park 904, 1098 XH Amsterdam, The Netherlands

<sup>§</sup>Department of Chemistry, Colorado State University, Fort Collins, Colorado 80523-1872, United States

making and -breaking reactions. <sup>13–17</sup> However, while redoxactive ligand complexes have found some applications in basemetal catalysis, <sup>18–42</sup> in most cases advancements are still needed to make these preformed complexes competitive with catalysts generated in situ from base-metal salts, reductants, and potential ligand additives. <sup>5,43–57</sup> Successes in rational basemetal catalyst design often begin with robust, tunable ligands. For instance, the redox-active bis(imino)pyridine [NNN] pincer ligands <sup>58,59</sup> were termed "privileged" because of their utility in Fe and Co catalysis. <sup>60</sup> Accordingly, elaborating a library of ligands that stabilize low-coordinate, later 3d metals across two or more formal oxidation states is a first step toward designed base-metal complexes for sustainable catalysis.

Previous results from the Soper laboratory have explored redox-active ligand aminophenol Co complexes for Negishitype cross-couplings of unactivated alkyl halides with alkyl- or arylzinc halides (Scheme 1).<sup>61,62</sup> Both the C–X oxidative

#### Scheme 1

addition and C-C reductive elimination steps apparently occur via Pd-like concerted two-electron steps. However, catalytic turnover is limited because C-C reductive elimination from the putative high-valent dialkyl/aryl intermediate cobalt complexes is inhibited by energetically unfavorable isomerization of the square-planar bis(amidophenolate) ligand field. This precludes access to the *cis* sites required for C-C elimination.

To address these issues, we sought a system that would capture the redox-active amidophenolate fragments within a *mer* pincer-type tridentate ligand scaffold. In this regard, the previously reported diphenolate imidazolyl carbene appeared promising. As shown in Scheme 2, the [OCO] pincer contains two di-*tert*-butylphenolate moieties flanking a central N-heterocyclic carbene (NHC) core. Beyond constraining the coordination geometry to open *cis* coordination cites for oxidative addition and reductive elimination transformations, we envisioned the NHC conferring other advantages. The strongly  $\sigma$  donating carbene makes the ligand less labile in its

#### Scheme 2

oxidized forms, and the increased electron density facilitates oxidative addition at the coordinated metal center. Its significant *trans* influence also enhances the lability of auxiliary ligands, <sup>64,65</sup> which is particularly beneficial for generating catalytically relevant species at substitutionally inert metal centers such as Co(III). Finally, the modular synthesis allows both of the lateral moieties as well as the medial NHC core to be easily modified, offering significant steric and electronic tunability. <sup>66,67</sup>

This OCO ligand has been reported on metals including Ti, Zr, Hf, V, Mn, Ir, Ni, Pd, Pt, and Al. 63,68-72 Most of these reports formulate the ligand as a bis(phenolate) dianion, but two previous papers discussed an expanded redox capacity. 70,72 Bercaw and co-workers described one- and two-electron oxidations of an [(OCO)Ir<sup>III</sup>Cl(PCy<sub>3</sub>)<sub>2</sub>] complex and suggested the possibility of a ligand-centered radical in the oxidized However, the solution electron paramagnetic materials.7 resonance (EPR) data did not permit definitive assignment of the oxidized species as metal-centered (OCO<sup>2-</sup>)Ir<sup>IV/V</sup> or ligand radical complexes (OCO • -) Ir III/IV. Ligand-centered oxidations were similarly invoked to rationalize the electrochemical and EPR data for oxidized homoleptic bis(OCO) ligated group 4 metals Ti, Zr, and Hf, but no structural data were reported and the putative ligand radical complexes were not isolated.

Reported herein are data for three new cobalt electron transfer series, each spanning four formal oxidation states. Structural data are presented that unambiguously show the OCO pincer ligands are redox centers in the highly oxidized complexes, and computational data support their assignments as ligand-centered radicals. Furthermore, variations in the NHC backbone saturation are shown to modulate the redox potential of the ligand-centered oxidations by over 400 mV, providing a convenient handle to tune these ligands for applications in small-molecule redox catalysis.

# RESULTS

**Diphenolate NHC Ligands.** The chloride salts of three tridentate pincer proligands featuring two di-*tert*-butylphenolate moieties on a central N,N'-disubstituted imidazole  $[H_3(OCO)-C1]$ , imidazoline  $[H_3(^SOCO)C1]$ , or benzimidazole  $[H_3(^{Ph}OCO)C1]$  core, were synthesized via slight modifications of previously reported procedures. The saturated variant  $[H_3(^SOCO)C1]$  was prepared in 82% yield from triethyl orthoformate promoted cyclization of N,N'-bis(2-hydroxy-3,S-di-*tert*-butylphenyl)ethylenediamine in the presence of concentrated hydrochloric acid  $(Scheme\ 3a).^{68,73}$  Analogous

#### Scheme 3

reaction of the *o*-phenylenediamine precursor afforded  $[H_3(^{Ph}OCO)Cl]$  in 79% yield. The unsaturated NHC core,  $[H_3(OCO)Cl]$ , was prepared according to a previously reported method by treating the diimine precursor with paraformaldehyde and TMSCl in ethyl acetate at 70 °C for 6 h (Scheme 3b).  $^{63,73}$ 

Synthesis and Structures of Reduced [OCO] Cobalt Complexes. The cobalt complexes 1–3, [(SOCO)-Co<sup>II</sup>(MeCN)], [(OCO)Co<sup>II</sup>(MeCN)], and [(PhOCO)-Co<sup>II</sup>(MeCN)], respectively, were prepared by a general method wherein the corresponding ligands were deprotonated with 3 equiv of NaOMe and subsequently treated with stoichiometric CoCl<sub>2</sub> (Scheme 4). As described below, the Co-pincer

#### Scheme 4

complexes bind an additional solvent-derived ligand upon workup, resulting in four-coordinate complexes. Samples isolated from MeCN or THF solutions vary in color from orange to red, and the isolated yields ranged from 88 to 93%. Suspending THF-derived samples in MeCN and adding the minimal amount of toluene required to completely dissolve the sample afforded analytically pure needle crystals of the corresponding MeCN complexes (Chart 1), implying that the THF ligands are labile.

Recrystallization of the complexes from concentrated MeCN solutions at -25 °C afforded crystals suitable for analysis by X-ray diffraction. As shown in Figure 1, the gross geometric features are consistent across the series. In each case, the four-coordinate Co center has approximate square-planar geometry, with the diphenolate carbene pincer ligand occupying three meridional sites and a solvent-derived MeCN ligand bound *trans* to the carbene.

Unsaturation in the ligand backbone leads to variations in the Co-ligand bonding metrics as well as the overall planarity of the complexes. Selected bond lengths are collected in Figure 2. The saturated imidazoline backbone of 1 twists the ligand backbone, as evidenced by the C2-N1-C3-N2 torsion angle of 5.72(1)°. The phenolate arms of 1 are displaced below the cobalt, causing the O1-Co-O2 and C3-Co-N3 bite angles to slightly contract to 170.3(1) and 172.2(1)°, respectively (Figure 1a, bottom). In contrast, the sp² carbons in the

imidazole backbone of 2 inhibit rotation along the C16–C17 bond, making the ligand coplanar with the Co center. In the solid state, the complex resides on a crystallographic mirror plane (Figure 1b, bottom). The benzimidazole complex 3 exhibits significant puckering about the Co center, causing both phenolic oxygen atoms to bend 7.2° above the N3–Co–C1 plane. The benzimidazole backbone is lifted out of plane (Figure 1c, bottom). The C–C bonding metrics about the flanking phenolate groups are statistically indistinguishable within the rings, across all complexes 1–3 (Figure 2), consistent with formulation of the phenolate substituents as fully reduced phenoxides,<sup>75</sup> from which we conclude that the NHC ligands are dianionic and the Co centers adopt a formal +II oxidation state.

The Co-O bond distances remain constant across the series, averaging  $1.811 \pm 0.005$  Å, and are in line with Co-O<sub>phenoxide</sub> distances in low-spin square-planar Co(II) centers supported by salen-type ligands. <sup>76–79</sup> A search of the CCDC in June 2017 revealed that all three Co1-C3 bond lengths (1.811(2)-1.830(8) Å) are substantially shorter than those in previously reported Co-NHC complexes (1.9135(19)-2.152(6) Å), 80-8 likely reflecting both the strong  $\sigma$ -donor ability of the NHC as well as geometric constraints imposed by the chelating phenolate arms. Notably, unsaturation in the backbone leads to a statistically significant elongation of the Co-C<sub>NHC</sub> distances along with a contraction of the Co-N bonds to the MeCN ligands and lengthening of the nitrile C≡N bonds (Figure 3). These bonding patterns can be rationalized by invoking enhanced  $\pi$  back-donation from the Co center to the saturated carbene in 1 vs 2 and 3, consistent with previous suggestions that imidazoline-derived NHCs are better  $\pi$ acceptors than their unsaturated imidazole counterparts. 65,86 However, nitriles are poor  $\pi$  acceptors, and similar effects might be expected only on the basis of the relative  $\sigma$ -donor abilities of the varying NHCs.

All three complexes are paramagnetic, as evidenced by the observation of broad, shifted  $^1H$  NMR spectra and the solution magnetic moments ( $\mu_{\rm eff}$ ) of 1.88, 1.82, and 1.90 for 1–3 in THF- $d_8$ , respectively. These measured moments are slightly higher than the spin-only values for an S=1/2 center, but square-planar Co(II) species are well-known to have significant contributions from the angular momentum term, L, typically leading to higher than spin-only values of  $\mu_{\rm eff}$ . The measured moments match those previously reported for low-spin square-planar Co(II) complexes. The observed magnetism is therefore consistent with a  $d^7$  configuration with a single unpaired electron.

**Electrochemistry.** Cyclic voltammograms of 1–3 were obtained in MeCN solutions containing 0.1 M tetra-n-butylammonium hexafluorophosphate ([<sup>n</sup>Bu<sub>4</sub>N][PF<sub>6</sub>]) as the supporting electrolyte. As shown in Figure 4, all three

Chart 1. MeCN Adducts of Complexes 1-3

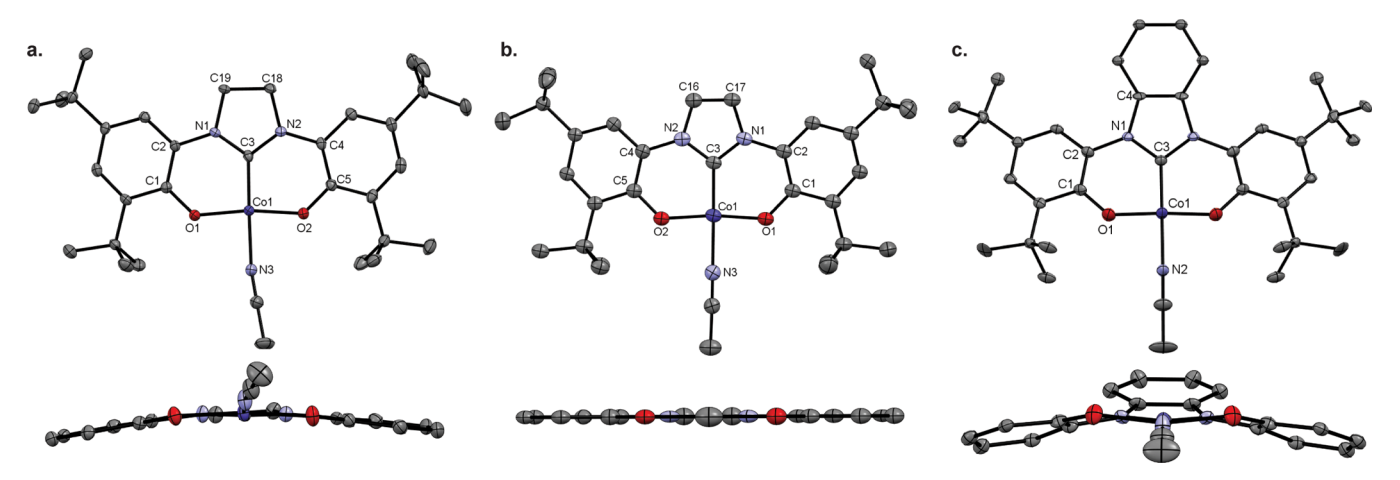


Figure 1. ORTEP plots of complexes (a)  $[(^{S}OCO)Co(MeCN)]$  (1), (b) [(OCO)Co(MeCN)] (2), and (c)  $[(^{Ph}OCO)Co(MeCN)]$  (3), as viewed from above (top) and down the Co1-C3 bond (bottom). Ellipsoids are drawn at 50% probability. Hydrogen atoms and noncoordinated acetonitrile molecules are omitted for clarity.

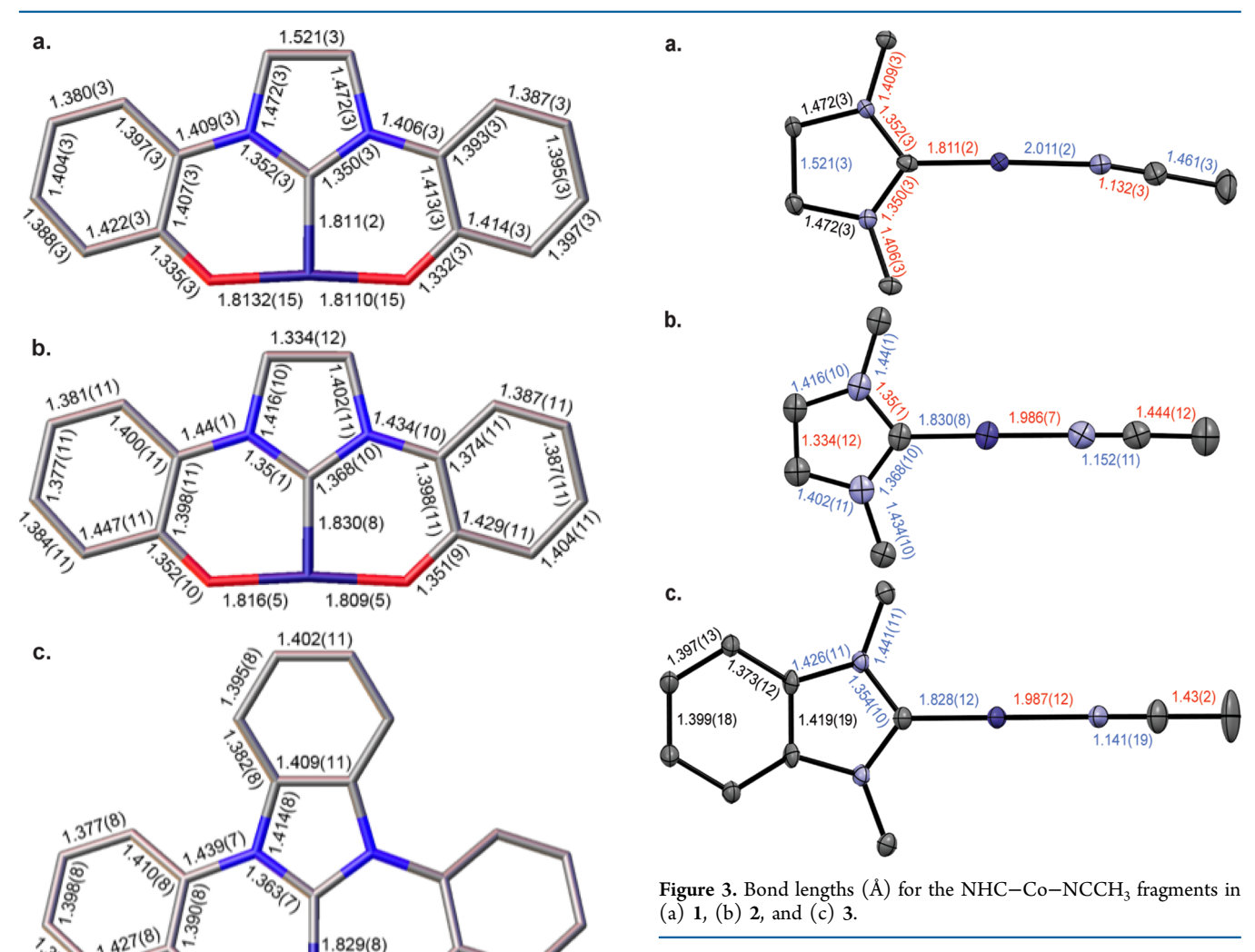
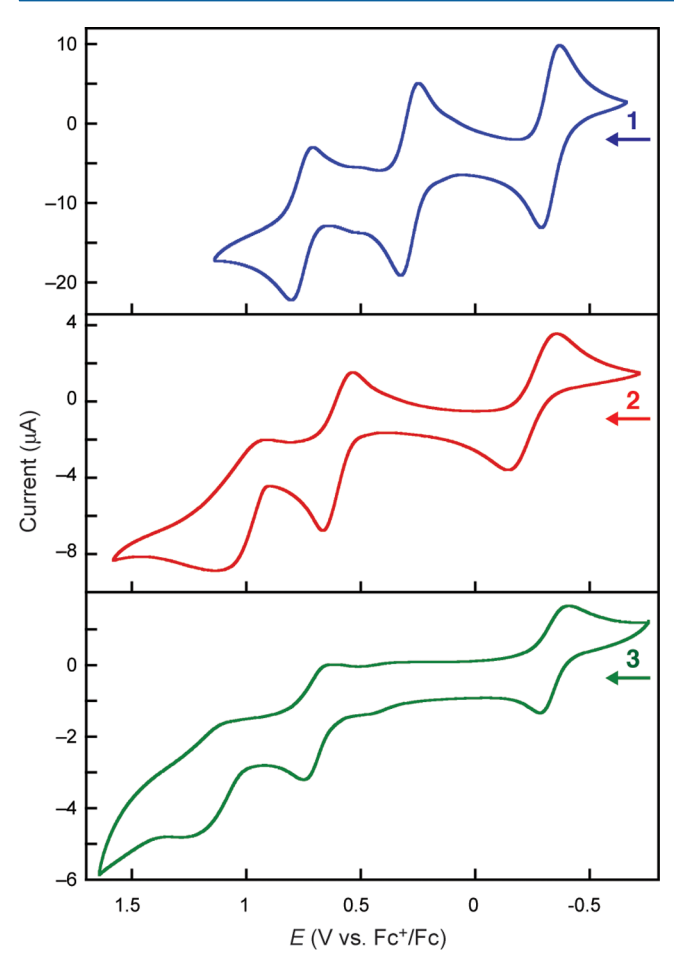


Figure 2. Schematic of selected bond lengths (Å) for complexes (a) 1, (b) 2, and (c) 3 drawn to correspond to Figure 1.

1.809(4)

complexes show three quasi-reversible 1e oxidations between -0.5 and +1.5 V vs Fc $^+$ /Fc. The potentials are collected in

Table 1. Substitutions in the NHC backbone minimally affect the position of the first oxidation,  $E_{1/2}^{-1}$ , which varies less than 95 mV between the most (3) and the least easily oxidized (2). However, the second and third oxidations,  $E_{1/2}^{-2}$  and  $E_{1/2}^{-3}$ , are strongly influenced by (un)saturation of the NHC backbone. For example, in the saturated NHC complex 1, the second oxidation event,  $E_{1/2}^{-2}$ , occurs nearly 300 mV more negative of the unsaturated imidazole-derived complex 2 and nearly 400



**Figure 4.** Cyclic voltammograms of 1 (blue), 2 (red), and 3 (green) in MeCN. Conditions: 5 mM 1–3, 0.1 M  $[Bu_4N][PF_6]$ , 1.0 mm Pt electrode, 100 mV s<sup>-1</sup> scan rate.

Table 1. Redox Potentials (V vs Fc+/Fc) of 1-3

complex	$E_{1/2}^{1} \left(\Delta E_{\rm p}\right) X/X^{+}$ couple	$E_{1/2}^2 \left(\Delta E_{\rm p}\right) \text{ X}^+/\text{X}^{2+}$ couple	$E_{1/2}^{3} (\Delta E_{\rm p}) X^{2+}/X^{3+}$ couple
1	-0.322 (0.086)	0.299 (0.085)	0.773 (0.108)
2	-0.252 (0.208)	0.596 (0.138)	0.963 (0.169)
3	-0.344 (0.132)	0.694 (0.105)	1.187 (0.189)

mV below the benzimidazole NHC complex 3. Similar trends are observed in the  $E_{1/2}^{-3}$  values spanning a range of over 400 mV, with 1 < 2 < 3.  $E_{1/2}^{-2}$  and  $E_{1/2}^{-3}$  represent the formation of complexes two and three redox levels above Co(II). However, as discussed below, the relative scarcity and presumed oxidizing power of molecular Co(IV) and Co(V) complexes led us to consider alternative formulations containing ligand-centered radicals. In this context, the observed  $E_{1/2}^{-2}$  and  $E_{1/2}^{-3}$  values are well within the range of reported ligand oxidations in complexes containing aryl oxide chelates (0.33–1.04 V vs Fc+/Fc) that generate phenoxyl radicals.

Synthesis and Structures of the  $[(OCO)Co(THF)_n]X_{n-1}$  (n = 1-3) Electron Transfer Series. To better understand the structural properties of the high-valent Co complexes observed in the cyclic voltammograms, chemical oxidations of 1 were performed in THF. Treating a dark orange, air-sensitive THF solution of 1 with 1 equiv of AgOTf afforded a dark green solution from which  $1^+$  was isolated as an air-stable green solid in 92% yield. A sample suitable for X-ray diffraction was

prepared by salt metathesis with NaBPh<sub>4</sub> followed by recrystallization from solvent diffusion of pentane into a concentrated THF solution at -25 °C. The structure of  $1^+$  is presented in Figure 5b. For comparison, an X-ray structure of a

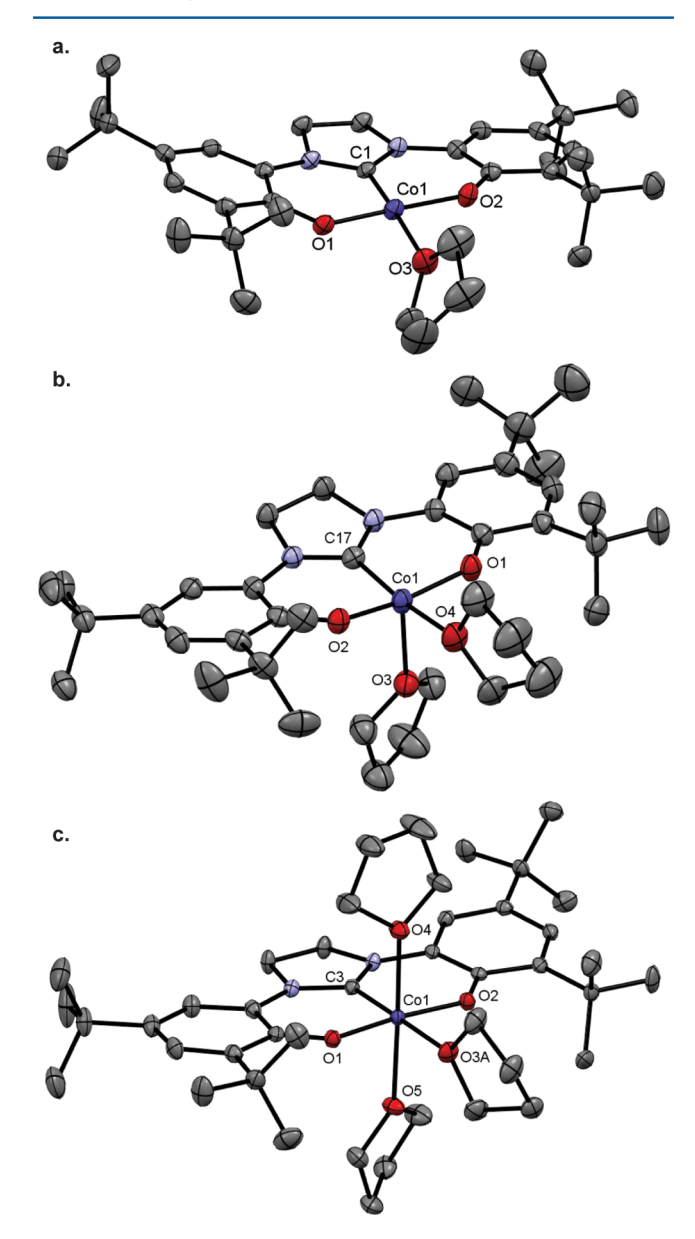


**Figure 5.** ORTEP plots of complexes (a) [( $^{S}OCO$ )Co(THF)] (1), (b) [( $^{S}OCO$ )Co(THF) $_{2}$ ][BPh $_{4}$ ] (1 $^{+}$ ), and (c) [( $^{S}OCO$ )Co(THF) $_{3}$ ]-[PF $_{6}$ ] $_{2}$  (1 $^{2+}$ ). Ellipsoids are drawn at 50% probability. Hydrogen atoms, counteranions, and noncoordinated solvent molecules are omitted for clarity.

sample of 1 isolated from THF is shown in Figure 5a. Bond length data in Figure 6a show that, with the exception of Co–C1 bond contraction from 1.811(2) to 1.790(4) Å, the structural perturbations in 1 are minimal on substitution of MeCN for THF.

The Co center in  $1^+$  is five-coordinate (Figure 5b), with the pincer ligand occupying three *mer* sites. Two THF ligands complete the pseudo-square-pyramidal geometry with a  $\tau$  value of 0.13 (cf.  $\tau$  = 0 for a perfect square pyramid and  $\tau$  = 1 for a perfect trigonal bipyramid). Oxidation of 1 to  $1^+$  occurs with contractions of each Co–O and O–C<sub>Ar</sub> bond by ca. 0.01 Å

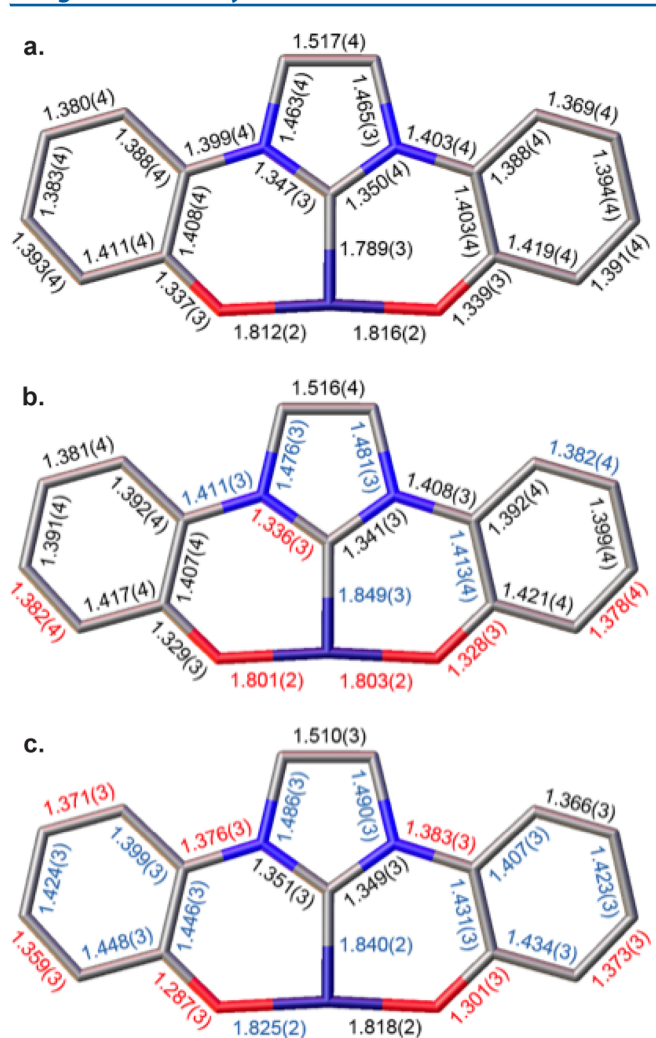


**Figure 6.** Schematic of selected bond lengths (Å) for complexes (a) 1, (b)  $1^+$ , and (c)  $1^{2^+}$ . Bond length changes greater than 0.01 Å in comparison to the fully reduced species, 1, are indicated by colored labels: red indicates bond contraction; blue indicates bond elongation.

each, and the Co–C1 bond to the carbene is lengthened from 1.789(2) Å in 1 to 1.849(3) Å (Figure 6b). All of the C–C bonds within the phenolate rings are indistinguishable from 1 within the error of the X-ray measurement, but both rings in 1<sup>+</sup> display distinctive quinoid-type bond alternations typical of those expected for phenoxyl radicals,<sup>75</sup> suggesting some degree of ligand oxidation might be operative.

THF solutions of  $1^+$  are paramagnetic with a solution moment ( $\mu_{\rm eff}$ ) of 2.88, consistent with the spin-only value for an S=1 center. The sum of these data are therefore consistent with formulation of  $1^+$  as either  $[(^S{\rm OCO}){\rm Co^{III}}({\rm THF})_2]^+$  containing a closed-shell  $[^S{\rm OCO}]^{2-}$  bis(phenolate) ligand on an intermediate-spin Co(III) center or  $[(^S{\rm OCO}^{\bullet}){\rm Co^{II}}({\rm THF})_2]^+$  with a low-spin Co(II) ion ferromagnetically coupled to an oxidized monoanionic  $[^S{\rm OCO}^{\bullet}]^-$  fragment containing a single unpaired electron distributed across the  $[{\rm OCO}]$  framework. The X-ray metrical data alone are insufficient to distinguish these possibilities, but computational and solid-state magnetism data discussed below are informative in this regard.

The dication  $1^{2+}$  was prepared from 1 by treatment with 2.1 equiv of  $[N(p-C_6H_4Br)_3][PF_6]$  in THF, giving immediate conversion to a dark green solution and a green-brown powder

upon workup. Crystals of 12+ suitable for single-crystal X-ray analysis were obtained by diffusion of pentane into a concentrated THF solution at -25 °C. Three THF molecules complete the coordination sphere about a pseudo-octahedral Co center (Figure 5c). Examination of the ligand metrical data (Figure 6c) shows a clear quinoid-type pattern of four long and two short C-C bonds in both phenoxide moieties. Additionally, the  $C_{Ar} \!\! - \!\! O$  and  $C_{Ar} \!\! - \!\! N$  bond lengths are contracted by an average of 0.044(4) and 0.022(5) Å, respectively, in comparison to 1, in line with the contractions expected upon oxidation of the phenoxide arms to phenoxyls. In total, the sum of the ligand data clearly contrast with those in 1 or 1<sup>+</sup> and are most consistent with formulation of the ligand in  $1^{2+}$  as a charge-neutral doubly oxidized SOCO ligand. Charge balance implies that the Co center is in the +II oxidation state; therefore, the complex is formulated as [(SOCO0)-Co<sup>II</sup>(THF)<sub>2</sub>]<sup>2+</sup>. The measured THF solution magnetic moment  $(\mu_{\text{eff}})$  of 2.51 is substantially above that expected for an S = 1/2ion-suggestive of substantial orbital contributions to the magnetic moment—but well below the spin-only moment for three or more unpaired spins. As discussed below, this could reflect multiple contributors to the ground state of 12+. However, 1<sup>2+</sup> is also prone to degradation to undefined Co species in solution at ambient temperature, thus complicating magnetic measurements, and hence this piece of magnetic data should be interpreted with caution.

All attempts to synthesize the  $1^{3+}$  complex observed in the CV were unsuccessful. The use of strong oxidants such as  $N(p-C_6H_4Br)_3^+$  and  $NO^+$  salts provided only an intractable mixture of products.

**Solid-State Magnetic Properties.** Magnetic susceptibility data were collected for 1 and 1<sup>+</sup> in the temperature range 2–300 K (Figure 7). For 1, the  $\chi_{\rm M}T$  value is 0.55 cm<sup>3</sup> K mol<sup>-1</sup>

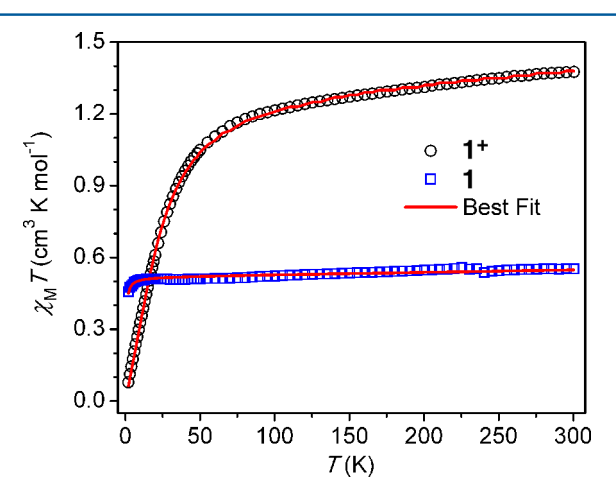


**Figure 7.** Temperature dependence of magnetic susceptibility for  $[(^{5}OCO)Co(THF)]$  (1) and  $[(^{5}OCO)Co(THF)_{2}](OTf)$  (1<sup>+</sup>), collected at 5 and 1 kOe, respectively. The best fits to the data were determined using PHI.<sup>90</sup>

 $(\mu_{\rm eff}=2.10~\mu_{\rm B})$  at 300 K, slightly higher than the spin-only value for a low-spin Co(II) species ( $S=1/2,~0.375~{\rm cm}^3~{\rm K}~{\rm mol}^{-1},~g=2$ ). When the temperature is decreased to 10 K, the  $\chi_{\rm M}T$  product decreases monotonically down to 0.50 cm<sup>3</sup> K mol<sup>-1</sup> ( $\mu_{\rm eff}=2.00~\mu_{\rm B}$ ), and upon further cooling to 2 K,  $\chi_{\rm M}T$  decreases more sharply to 0.45 cm<sup>3</sup> K mol<sup>-1</sup> ( $\mu_{\rm eff}=1.9~\mu_{\rm B}$ ). The susceptibility data were fit successfully to an S=1/2 model using PHI;<sup>50</sup> the magnetic parameters are shown in Table 2.

Table 2. Magnetic Parameters for [(SOCO)Co(THF)] (1) and [(SOCO)Co(THF), ](OTf) (1+)

compound	g	$\Theta$ (cm <sup>-1</sup> )	$D(E)(cm^{-1})$	$J \text{ (cm}^{-1})$	TIP $(10^{-6} \text{ cm}^3 \text{ mol}^{-1})^a$	$R^2$
[(°OCO)Co(THF)]	2.33	-0.11			150	0.9998
[(°OCO)Co(THF) <sub>2</sub> ](OTf)						
model 1	2.56			-10.3	600	0.9962
model 2	2.24		$62.1 (20.7)^{b,c}$		400	0.9976
model 3	2.18		$-40.3 (13.4)^c$	-252	400	0.9988

"In PHI, temperature-independent paramagnetic susceptibility (TIP) is added to the data but is not a fitted parameter. <sup>b</sup>Note that the signs of anisotropy parameters are not reliably determined from fits to susceptibility data, but a positive D value is consistent with population of an  $M_S = 0$  microstate as T approaches zero, as observed in the experimental data. <sup>c</sup>Anisotropy values were adjusted according to a literature procedure to ensure that  $|E| \le |D|/3$ .

The isotropic g value obtained from the fit is similar to that found via EPR spectroscopy (vide infra) and is reasonable considering the large intrinsic spin—orbit coupling in previously characterized low-spin Co(II) species;  $^{91,92}$  free refinement of  $g_{xv}$   $g_{yv}$  and  $g_z$  do not improve the overall fit quality and do not agree with EPR simulations (Table S37 in the Supporting Information). Inclusion of a mean field correction ( $\Theta$ ) improved the fit, consistent with weak intermolecular antiferromagnetic coupling, likely from  $\pi$  stacking through [SOCO] ligands on adjacent species as shown in the crystal-packing diagram (Figure S9 in the Supporting Information). The field dependence of magnetization (Figure S10 in the Supporting Information) shows near-saturation of magnetization at  $\sim$ 1.1 N  $\mu_{\rm B}$ , consistent with one unpaired electron in the ground state.

The magnetic properties of the mono-oxidized compound 1<sup>+</sup> offer several interpretations. This complex displays a roomtemperature magnetic susceptibility value of 1.38 cm<sup>3</sup> K mol<sup>-1</sup>  $(\mu_{\text{eff}} = 3.0)$ , consistent with an S = 1 species (1.00 cm<sup>3</sup> K mol<sup>-1</sup> expected for g = 2). Upon cooling, a gradual linear decrease is observed: at 50 K, the  $\chi_{\rm M}T$  product is 1.05 cm<sup>3</sup> K mol<sup>-1</sup> ( $\mu_{\rm eff}$  = 2.90). A more pronounced decrease is observed upon further cooling, and at 2 K  $\chi_{\rm M}T$  is 0.08 cm<sup>3</sup> K mol<sup>-1</sup> ( $\mu_{\rm eff}=0.79$ ). The near zero magnetization at 2 K increases very slowly as the field is increased to 5 kOe (Figure S11 in the Supporting Information) and does not show any tendency toward saturation, consistent with a relatively well isolated  $M_S = 0$ microstate at low temperatures. On the basis of these data, several spin distribution scenarios are feasible: (1) low-spin Co(II) antiferromagnetically coupled to a ligand radical, (2) intermediate-spin Co(III) center or ferromagnetic coupling between a low-spin Co(II) and a ligand radical, or (3) high-spin Co(II) antiferromagnetically coupled to a ligand radical. The first scenario would give a net S = 0 ground state, whereas the other models would give net S = 1 ground states but with large anisotropy such that the  $M_S = 0$  microstate is populated at lowest temperatures. The data were fit to several models using PHI; all fit parameters are collected in Table S38 in the Supporting Information. Model 1 did not provide reasonable g or coupling parameters; importantly, curvature in the simulated  $\chi_{\rm M}T$  values does not agree with the linear decrease observed at the lowest temperatures probed (Figure S12 in the Supporting Information). In contrast, models 2 and 3 provide reasonable g values as well as large zero-field splitting (D) values. The presence of significant axial anisotropy is consistent with the shape of the downturn at low temperatures. Model 3 also gave a large negative I value, consistent with strong antiferromagnetic coupling between a putative high-spin Co(II) center and a ligand radical. On the basis of these fits, it is likely that 1+ contains an intermediate-spin Co(III) center or a high-spin

Co(II) center antiferromagnetically coupled to a ligand radical. To definitively differentiate models 2 and 3, much higher measuring temperatures and/or high fields would be needed. However, on comparison to fits to the high-temperature data (Figure S12), the "intermediate spin" model (2) follows the linear increase in  $\chi_{\rm M}T$ , whereas the "antiferromagnetic coupling" model (3) shows slight curvature. Thus, given the current data, model 2, a highly anisotropic triplet, offers the best agreement with data. Whether this is localized on the "Co(III)" ion or is the result of exceptionally strong ferromagnetic coupling between low-spin Co(II) and a ligand radical cation cannot be distinguished from the current data.

**EPR Spectroscopy.** The X-band EPR spectrum of a THF-derived sample of 1 was obtained in toluene glass at 20 K (Figure 8). It displays a rhombic signal with well-resolved

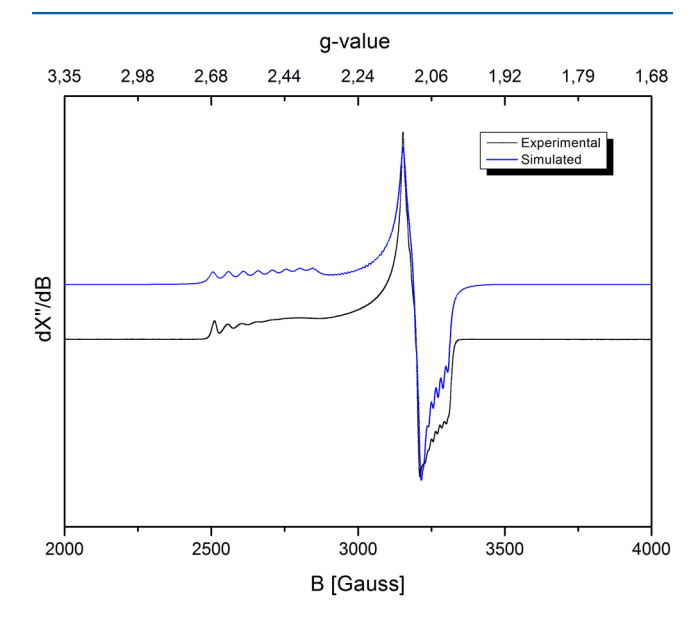


**Figure 8.** X-band EPR spectrum of a THF-derived sample of **1** in toluene glass at 20 K. Conditions: microwave frequency, 9.388589 GHz; power, 0.6325 mW; modulation amplitude, 2.000 G.

cobalt hyperfine coupling interactions (HFIs) along two directions of the **g** tensor. The spectrum is characteristic for a metalloradical S=1/2 system, with the unpaired electron being localized mainly at the cobalt center. A satisfactory simulation of the experimental spectrum was obtained with the EPR parameters shown in Table 3. Spin-unrestricted (collinear) spin—orbit DFT calculated EPR parameters are overall in reasonable agreement with the experimental values (Table 3). The DFT computed  $A^{\text{Co}}_{x}$  and  $A^{\text{Co}}_{y}$  HFI values are somewhat too high though, while the  $g_{z}$  value is underestimated. This is

Table 3. Experimental (Simulation) and DFT Calculated EPR Parameters of 1

	sim	$\mathrm{DFT}^a$
	g Tensor	
$g_x$	2.061	2.056
$g_y$	2.105	2.102
$g_z$	2.500	2.302
	Hyperfine Coupling (MHz	)
$A^{\operatorname{Co}}_{}x}$	45	+145
$A^{\text{Co}}_{y}$ $A^{\text{Co}}_{z}$	NR (<30)	+82
$A^{\text{Co}}_{z}$	170	-176

<sup>a</sup>ADF, B3LYP, TZ2P, unrestricted collinear spin-orbit calculations.

suggestive of a slightly overestimated DFT HOMO–SOMO energy gap, perhaps caused by solvation effects and/or concrete toluene solvent adduct formation at 20 K in the experimental system. <sup>94</sup>

As can be expected for a metal-based electronic triplet system (S = 1), with expected large zero-field splitting parameter D, the X-band EPR spectrum of  $\mathbf{1}^+$  measured in toluene glass at 20 K gave no signal in the range of 0–6000 G. The solution instability of  $\mathbf{1}^{2+}$  precluded measurement of an EPR spectrum.

Computed Electronic Structures of 1, 1<sup>+</sup>, and 1<sup>2+</sup>. The electronic structures of the THF adducts 1, 1<sup>+</sup>, and 1<sup>2+</sup> were computed with unrestricted DFT-D3 calculations (BP86, def2-TZVP, disp3), excluding counterions, and with starting spin states as determined experimentally. Optimized geometries were compared to the single-crystal X-ray structures and found to have maximum bond length deviations of 0.023, 0.023, and 0.026 Å for 1, 1<sup>+</sup>, and 1<sup>2+</sup>, respectively, suggesting that the spin states, functional, and basis set (BP86, def2-TZVP, disp3) used in the geometry optimizations accurately capture the bond distances in the [SOCO] ligands across all three formal oxidation states. The spin densities per atom in optimized geometries were also calculated. Accordingly, complex 1 converged as a doublet ( $\langle s^2 \rangle = 0.7611$ ), with 81% of the total spin density being located at cobalt (Figure 9). Some residual

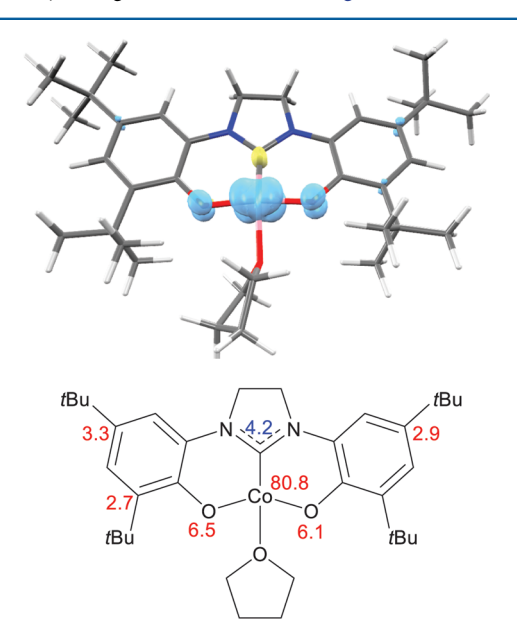


**Figure 9.** (top) Spin density plot of 1 (S = 1/2), generated with IQMol (isosurface value 0.005). (bottom) Spin density per atom for the THF adduct of 1 (S = 1/2).

spin density is delocalized over both phenoxide arms of the OCO ligand, mainly on the oxygen atoms (total of 12.6%). A small amount of spin-down density is observed on the NHC carbon center (4.2%), which can be attributed to spin polarization. The computed structure of 1 is therefore best described as  $[(^SOCO)Co^{II}(THF)]$ , with a closed-shell  $[^SOCO]^{2-}$  dianion on a low-spin Co(II) center.

 $1^+$  converged as a triplet  $(\langle s^2 \rangle = 2.0156)$ . The involvement of a quintet state  $(\langle s^2 \rangle = 6.0132)$  is highly unlikely, as this state is computed to be +20 kcal mol<sup>-1</sup> uphill vs the triplet state. However, the singlet state is found to be only +5 kcal mol<sup>-1</sup> above the triplet state, and the open-shell singlet state is only +4 kcal mol<sup>-1</sup> uphill from the triplet state. In the triplet state, 66% of the electron density is localized at Co; the remainder is delocalized over the phenoxide moieties (Figure 10). These

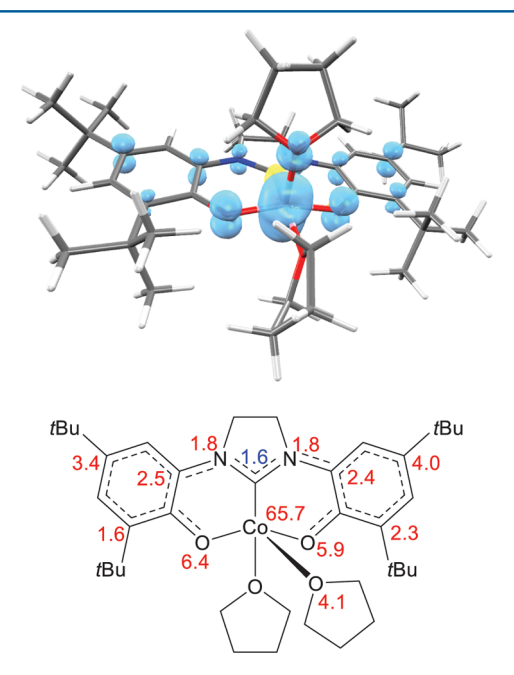
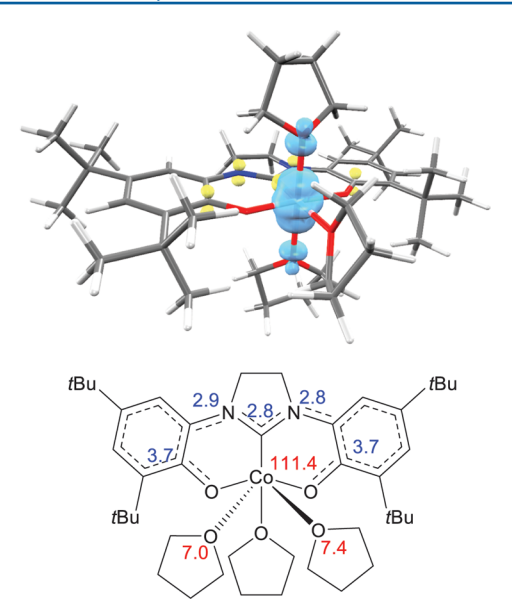


Figure 10. (top) Spin density plot of  $1^+$  (S=1), generated with IQMol (isosurface value 0.005). (bottom) Spin density per atom for the bis-THF adduct of  $1^+$  (S=1).

data are most consistent with description of  $\mathbf{1}^+$  as containing a Co(II) center supported by a monooxidized  $[^SOCO^{\bullet}]^-$  ligand radical. However, the accessibility of multiple low-lying excited states suggests that other contributors to the ground state might need to be considered (perhaps requiring multireference calculations, beyond the scope of the present study).

Complex  $1^{2+}$  converged as a doublet  $(\langle s^2 \rangle = 0.8342)$ . The spin density of  $1^{2+}$  is almost entirely localized at the cobalt center, with some spin polarization causing some negative spin population on the NHC ligand atoms (and hence more than 100% positive spin at cobalt; Figure 11). Unrestricted natural and corresponding orbital analysis of the  $\alpha$  and  $\beta$  molecular orbitals revealed the presence of only one  $\alpha$  MO without (large) overlap with a corresponding  $\beta$  MO (UCO overlap values of all other  $\alpha$  and  $\beta$  MO pairs >0.96). Accordingly, the computational data suggest that the complex is best described as  $[(^{S}OCO^{0})Co^{II}(THF)_{3}]^{2+}$ , with a single unpaired electron localized on the  $d^{7}$  Co(II) center and a doubly oxidized, chargeneutral, and closed-shell diamagnetic  $^{S}OCO^{0}$  ligand (Figure 12a). While the  $^{S}OCO^{0}$  ligand could in principle be described as a singlet diradical with very strong antiferromagnetic



**Figure 11.** (top) Spin density plot of  $1^{2+}$  (S = 1/2), generated with IQMol (isosurface value 0.005). (bottom) Spin density per atom for the tris-THF adduct of  $1^{2+}$  (S = 1/2).

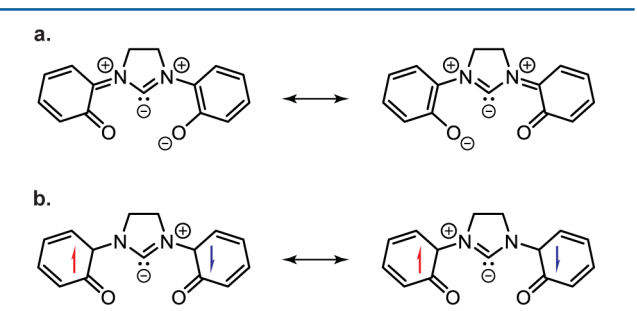


**Figure 12.** Key resonance structures of the closed-shell (a) and openshell singlet (b) configurations of the doubly oxidized, charge-neutral  $^{S}OCO^{0}$  ligand. The closed-shell representation (a) prevails according to DFT.

coupling between the two conjugated ligand-radical electrons (Figure 12b), there are actually no indications for such a (broken-symmetry) electronic structure with multiple unpaired electrons. Complex 1<sup>2+</sup> contains only one unpaired electron according to DFT, which is located at cobalt.

# DISCUSSION

Physical Oxidation States in the (OCO)Co Electron Transfer Series. The bis(phenolate) NHC cobalt complexes reported herein span a remarkably broad range of redox states. Cyclic voltammograms of complexes 1-3 all show three quasi-reversible one-electron oxidations at <1.2 V vs Fc $^+$ /Fc. These formally correspond to the generation of Co(III), Co(IV), and Co(V) in the mono-, di-, and trications, respectively. However, the combined experimental and computational data suggest that the physical oxidation states of cobalt are significantly lower.

Complex 1 is appropriately described as [(SOCO)-Co<sup>II</sup>(THF)], with a closed-shell [SOCO]<sup>2-</sup> dianion supporting a low-spin Co(II) center, and the unsaturated NHC variants 2 and 3 are formulated similarly. Exclusively four-coordinate quasi-square-planar structures were obtained for crystals of 1 grown from either THF or MeCN and for 2 and 3 grown from MeCN. Four-coordinate cobalt(II) complexes are most

commonly supported by tetradentate macrocycles, such as porphyrins or bis(Schiff base) bis(phenolate) N<sub>2</sub>O<sub>2</sub> salens. 76-78,96,97 However, square-planar Co(II) complexes of pincer [PNP] amidodiphosphine ligands have been recently described, 88 and the electronic structures of high-spin squareplanar Co(II) have been discussed. 98 Here, the reluctance of 1-3 to bind additional ligands is not attributable to sterics, as evidenced by the quasi-octahedral structure of [(SOCO0)-Co<sup>II</sup>(THF)<sub>3</sub>]<sup>2+</sup>, which is formulated analogously as a low-spin cobalt(II) ion. Rather, the preference for four-coordination in the lower oxidation states is apparently electronic in origin. In the absence of significant  $\pi$  bonding, the  $d_{x^2-y^2}$  orbital that is directed at the vacant coordination sites—when the z axis is colinear with the Co-C<sub>NHC</sub> bond—is half-filled in the low-spin d<sup>7</sup> configuration. Oxidizing the ligand does not change the electron count at Co; therefore, the preference for additional THF ligands in 12+ reflects increased Coulombic attraction to the dication (Figure S13 and Table S38 in the Supporting Information). This also accounts for the nearly invariant Co–O distances upon oxidation of 1 (Figure 6); increased charge counterbalances the decreased O-donor strength/basicity in the oxidized ligand.

Isolation of 1<sup>2+</sup> provides clear structural evidence for redox activity within the [OCO] pincer ligand. Although such ligand oxidations had been previously suggested, 70,72 this is to our knowledge the first isolated [OCO] pincer complex with an oxidized ligand. X-ray data for the doubly oxidized ligand are consistent with those expected for a diradical, but calculations show it is better formulated as a closed-shell SOCO diamagnet, implying the NHC mediates electronic communication across the [OCO] framework.

The electronic structure of the intermediate oxidation state 1<sup>+</sup> species defies simple assignment. As noted above, the solidstate structural and magnetic data can be reasonably interpreted as either  $[(^SOCO)Co^{III}(THF)_2]^+$  with a closed-shell  $[^SOCO]^2$ bis(phenolate) ligand on an intermediate-spin cobalt(III) center, or [(SOCO\*)Co<sup>II</sup>(THF)<sub>2</sub>]<sup>+</sup> with a low-spin Co(II) ion ferromagnetically coupled to a monoanionic [SOCO] ligand radical, containing a single unpaired electron distributed over the [OCO]  $\pi$  system. DFT calculations are more consistent with the latter formulation but reveal closed-shell singlet and open-shell singlet states at thermally accessible energies relative to the triplet (S = 1) ground state. In reality, the ground state of 1<sup>+</sup> might have multiple contributors. If the true electronic structure is indeed some combination of the formulations listed above, then the physical oxidation states of the metal and ligand should be highly susceptible to small perturbations in the solvent, temperature, and coordination environment, making the ligand truly noninnocent.9

**Effects of NHC Unsaturation on Ligand-Centered Oxidations.** The oxidized variants of 2 and 3 were not isolated, but given the structural homology in 1–3, it seems reasonable to assume that  $2^{2+}$  and  $3^{2+}$  also contain ligand radicals. So how do we rationalize the large (up to 400 mV) anodic shifts in the ligand-centered oxidations upon incorporation of unsaturation into the NHC ligand backbone? Two potential explanations were considered.

(1) Wolczanski and co-workers have recently suggested that the relative accessibility of ligand-centered oxidations can be understood by simple  $\pi$ -electron counting and the application of Hückel's rule. <sup>100,101</sup> By this logic, the [SOCO]<sup>2-</sup> ligand is a  $20e^-\pi$  system that becomes aromatic upon  $2e^-$  oxidation to SOCO<sup>0</sup> (see Figure 12a). The unsaturated [OCO]<sup>2-</sup> and

 $[^{Ph}OCO]^{2^-}$  ligands have 22 and 26  $\pi$  electrons, respectively, making them aromatic in their reduced forms; they should have a much lower propensity to be oxidized, which is consistent with the CV data. This argument implies that the unsaturated backbones in the imidazole- and benzimidazole-derived ligands are capable of delocalizing their  $\pi$  electrons across the entire [OCO] ligand. Previous literature has suggested that unsaturated imidazole-derived NHCs may <sup>102</sup> or may not <sup>103</sup> be aromatic. If the backbone  $\pi$  electrons are electronically decoupled from the rest of the [OCO] framework, then this rationale fails. The DFT results strongly point to full delocalization of the  $\pi$  system, in favor of aromaticity of the <sup>S</sup>OCO<sup>0</sup> ligand in 1<sup>2+</sup>.

(2) As detailed above, the varying Co–C bond distance across 1–3 might be ascribed to enhanced  $\pi$  back-donation from the cobalt(II) center in 1 to the NHC in comparison to 2 and 3. The saturated imidazoline-derived NHC is known to be a better  $\pi$  acceptor than the unsaturated (benz)imidazole NHCs. Enhanced back-bonding increases  $\pi$  electron density in the saturated [SOCO]<sup>2–</sup> ligand, thereby increasing its susceptibility to oxidations that generate phenoxyl radicals by removal of one or more  $\pi$  electrons.

A definitive explanation for the observed shifts in the ligand-centered oxidation potentials eludes us. It might in fact arise from a combination of the factors listed above. In contrast, the relative invariance in the first oxidation events across 1-3 is reasonably attributed to significant Co(III) character in  $1^+-3^+$ . From the perspective of the cobalt(II) center, the coordination environment is nearly uniform in all of 1-3, rendering a metal-centered oxidation relatively invariant to unsaturation or substitutions in the distal half of the NHC fragment.

[OCO] as a Platform for Multielectron Transformations at Co. The sum of the structural and electronic data presented above presents an exciting opportunity to develop new small-molecule reaction chemistry at [OCO] complexes. For instance, a list of design criteria for a new Co crosscoupling catalyst might include a low-coordinate complex in a low formal oxidation state, with a multielectron capacity that favors higher coordination numbers in higher oxidation states. In this respect, the [OCO] ligand seems ideally suited for such organometallic reactivity at later 3d metals. As shown herein, it stabilizes low-coordinate Co in low formal oxidation states, and higher formal oxidation states lead to higher coordination complexes. The (OCO)Co core is robust, but labile ancillary ligands afford multiple cis coordination sites for small-molecule binding and activation. Most importantly, the [OCO] framework gives access to oxidation states three levels above Co(II) at modest potentials. Accordingly, oxidative addition to Co(II) can be envisioned to occur without formation of high-energy Co(IV) species. Furthermore, unsaturation in the NHC backbone is shown to afford a high degree of electronic tunability, allowing the reducing power of the metal complexes to be tuned by up to 400 mV without significantly perturbing the coordination environment or sterics about the Co centers. These properties should be broadly transferrable to other organometallic catalysis cycles that utilize precious metals for multielectron bond activation and functionalization.

# CONCLUSIONS

Tridentate, *mer* pincer-type ligands are now ubiquitous in catalysis, and the [OCO] pincer appears to be well positioned to take a place alongside "privileged" ligands for base-metal catalysis, such as bis(imino)pyridine [NNN] pincers. <sup>60</sup> The

factors that make this system particularly attractive as a platform for new reaction chemistry include the capacity to stabilize Co over three or more formal oxidation states at relatively modest potentials, along with an impressive flexibility in coordination number and geometry. All of these are predicated on the capacity of the [OCO] ligand to persist in oxidation states that span multiple electrons. Although this redox capacity had been previously inferred, this report describes, to our knowledge, the first structurally characterized [OCO] ligand radicals and provides unequivocal proof for the redox activity of this ligand scaffold.

The [OCO] pincer ligands additionally show a remarkable and unexpected electronic tunability, with ligand-centered oxidations spanning over 400 mV depending on the degree of unsaturation in the NHC ligand backbone. Going forward, we posit that these properties will be broadly beneficial for the development of new methods for selective, organometallic-type small-molecule redox transformations at later 3d metals. The first efforts in our laboratory have focused on Co-mediated C—C coupling, but extensions to other classes of reactions, and other base metals, will be described in subsequent reports.

# EXPERIMENTAL DETAILS

General Considerations. Unless otherwise specified, all manipulations were performed under anaerobic conditions using standard vacuum line techniques or in an inert-atmosphere glovebox under purified nitrogen. Routine NMR spectra were acquired on either a Varian Mercury 300 spectrometer (300.323 MHz for <sup>1</sup>H; 75.5 MHz for <sup>13</sup>C) or a Varian Mercury 400 spectrometer (399.94 MHz for <sup>1</sup>H; 101.1 MHz for <sup>13</sup>C). All chemical shifts are reported in parts per million (ppm) relative to TMS, with the residual solvent peak serving as an internal reference. 104 Solution magnetic moments were obtained by the Evans NMR method 105,106 and are reported as the average of three independent measurements, unless otherwise specified. UVvisible absorption spectra were acquired using a Varian Cary 50 spectrophotometer. Unless otherwise noted, all electronic absorption spectra were recorded at ambient temperatures in 1 cm quartz cells. IR absorption spectra were obtained via attenuated total reflection (ATR) with a diamond plate using a Bruker ALPHA Fourier-transform infrared spectrophotometer. All mass spectra were recorded in the Georgia Institute of Technology Bioanalytical Mass Spectrometry Facility. Electrospray ionization mass spectrometry (ESI-MS) was carried out with acetonitrile solutions using a Micromass Quattro LC spectrometer. Electron impact mass spectra (EI-MS) were obtained using a VG Instruments Model 70-SE spectrometer. The EPR spectrum was recorded on a Bruker EMX X-band spectrometer equipped with a He cryostat. The spectrum was analyzed and simulated using the W95EPR program of Prof. F. Neese. Cyclic voltammetry experiments were performed inside an  $N_2$ -filled glovebox in MeCN with 0.1 M [<sup>n</sup>Bu<sub>4</sub>N][PF<sub>6</sub>] as the supporting electrolyte, unless otherwise noted. The voltammograms were recorded with a CH Instruments 620C potentiostat, using a 2.5 mm (o.d.) 1.0 mm (i.d.) Pt-disk working electrode, Ag-wire quasi-reference electrode, and a Ptwire auxiliary electrode, at a scan rate of 0.1 V s<sup>-1</sup>, unless reported otherwise. Reported potentials are referenced to the ferrocenium/ ferrocene (Fc+/Fc) redox couple, added as an internal standard at the conclusion of each experiment. Elemental analyses were performed by Atlantic Microlab, Inc., Norcross, GA. All analyses were performed in duplicate, and the reported compositions are the average of two runs. Full details of X-ray data collection and refinement are provided in the Supporting Information.

Methods and Materials. Anhydrous acetonitrile (MeCN), dichloromethane, pentane, tetrahydrofuran (THF), and toluene solvents for air- and moisture-sensitive manipulations were purchased from Sigma-Aldrich and further dried by passage through columns of activated alumina, degassed by at least three freeze-pump-thaw cycles, and stored under N<sub>2</sub> prior to use. Anhydrous methanol

(Drisolv) and benzene (Drisolv) were purchased from EMD Millapore and used as received. Deuterated solvents were purchased from Cambridge Isotope Laboratories. Acetonitrile- $d_3$  was dried over excess calcium hydride, vacuum-distilled to an oven-dried sealable flask, and degassed by successive freeze–pump—thaw cycles. Tetrahydrofuran- $d_8$  was used as received. The ligand precursors  $N_1N'$ -bis(2-hydroxy-3,5-di-tert-butylphenyl)ethylenediamine,  $^{73}$   $N_1N'$ -bis(2-hydroxy-3,5-di-tert-butylphenyl)phenylenediamine,  $^{74}$  and the ligand  $H_3[(OCO)]Cl^{63}$  were prepared according to published procedures.  $[N_1/2](P_1/2)(P_$ 

**Synthesis of** [ $H_3$ ( $^{S}$ OCO)]Cl. In a modified literature procedure,  $^{68}$  N,N'-bis(2-hydroxy-3,5-di-tert-butylphenyl)ethylenediamine (5.65 g, 12.1 mmol) was dissolved in (EtO) $_3$ CH (250 mL) and heated to 70  $^{\circ}$ C in air. Concentrated HCl (1.33 mL, 16.1 mmol) was added dropwise over 5 min, resulting in a color change from golden yellow to red-purple. After 15 min, a thick white precipitate formed and the stirring was increased to ensure even mixing. After it was stirred for 1 h, the reaction mixture was cooled to room temperature and filtered. The white solid was washed with copious Et<sub>2</sub>O (150 mL) and dried under high vacuum at 60  $^{\circ}$ C overnight (4.93 g, 9.56 mmol, 79%). All characterization data matched those previously reported.  $^{68}$ 

**Synthesis of** [ $H_3$ ( $^{Ph}$ OCO)]CI. In a modified literature method,  $^{74}$  N,N'-bis(2-hydroxy-3,5-di-tert-butylphenyl)phenylenediamine (3.52 g, 6.81 mmol) was dissolved in (EtO) $_3$ CH (150 mL) and heated to 70  $^{\circ}$ C in air. Concentrated HCl (0.84 mL, 10.2 mmol) was added dropwise over  $\sim$ 5 min, resulting in a color change from golden yellow to red-purple. After 15 min, a thick white precipitate formed and the stirring was increased to ensure even mixing. After it was stirred for 1 h, the reaction mixture was cooled to room temperature and filtered. The white solid was washed with copious Et<sub>2</sub>O (150 mL) and dried under high vacuum at 60  $^{\circ}$ C overnight (3.14 g, 5.58 mmol, 82%). All characterization data matched those previously reported.  $^{74}$ 

**Synthesis of 1–3.** The same general procedure was followed for all of 1–3. A 20 mL scintillation vial was charged with a solution of  $[H_3(^SOCO)]Cl$  (515 mg, 1.0 mmol) in MeOH (8 mL). NaOMe (5.4 M in MeOH, 555  $\mu$ L, 3.0 mmol) was added dropwise. The resulting yellow solution was stirred for 5 min and then added dropwise to a separate 20 mL vial containing anhydrous CoCl<sub>2</sub> (129.8 mg, 1.0 mmol) in MeOH (10 mL). The solution became dark red, and a redorange precipitate formed within 0.5 h. The suspension was stirred for an additional 6 h, and the solids were then separated by vacuum filtration.

Synthesis of [( $^{S}OCO$ )Co(MeCN)] (1). Following the above representative procedure, the collected solids were suspended in MeCN (5 mL) and a minimal amount of toluene was added to completely dissolve the material. This solution was stored at -25 °C for 18 h, producing orange crystals of 1 suitable for XRD analysis (507.5 mg, 0.88 mmol, 88%). Satisfactory elemental analysis required the inclusion of solvent-derived MeOH; the reported analysis is for [( $^{S}OCO$ )Co(MeCN)]·1.5MeOH. Anal. Calcd for C<sub>34.5</sub>H<sub>53</sub>CoN<sub>3</sub>O<sub>3.5</sub>: C, 66.33; H, 8.55; N, 6.73. Found: C, 66.84; H, 8.16; N, 6.23. UV–vis (MeCN;  $\lambda_{max}$ ) nm ( $\varepsilon$ , M<sup>-1</sup> cm<sup>-1</sup>)): 438 (5600). FTIR (ATR, cm<sup>-1</sup>): 2949(m), 2900(m), 2865(m), 1627(w), 1477(s), 1449(s), 1389(m), 1357(m), 1325(s), 1285(m), 1236(m), 1201(m), 1073(w), 982(w), 842(m), 760(m), 701(m), 678(m), 644(m), 579(m), 514(m), 434(m), 413(m).

*Synthesis of* [ $^{\circ}$ OCO)Co(THF)] (1). The THF adduct to 1 was obtained analogously using THF solvent in place of MeCN. Crystalline solids suitable for single-crystal X-ray diffraction were obtained by slow diffusion of pentane into a saturated THF solution at  $-20~^{\circ}$ C. UV—vis (THF;  $\lambda_{\text{max}}$ , nm ( $\varepsilon$ , M $^{-1}$  cm $^{-1}$ )): 430 (5300). FTIR (ATR, cm $^{-1}$ ): 2947(m), 2899(m), 2866(m), 1506(s), 1478(m), 1447(m), 1389(m), 1358(m), 1325(s), 1283(m), 1270(m), 1240(m), 1200(m), 1159(m), 1076(m), 1051(m), 914(m), 894(m), 869(m), 836(m), 756(m), 699(m), 643(m), 605(m), 578(m), 545(m), 512(m), 466(m), 434(m), 419(m).

*Synthesis of [(OCO)Co(MeCN)]* (2). The above representative procedure, followed by recrystallization from MeCN—toluene at -25 °C, afforded 2 as X-ray-quality crystals in 93% yield. Anal. Calcd for C<sub>33</sub>H<sub>45</sub>CoN<sub>3</sub>O<sub>2</sub>: C, 68.97; H, 7.89; N, 7.31. Found: C, 68.54; H, 7.78; N, 7.28. UV—vis (MeCN;  $\lambda_{\text{max}}$ , nm ( $\varepsilon$ , M<sup>-1</sup> cm<sup>-1</sup>)): 308 (23,000), 327 (2200), 418 (5100). FTIR (ATR, cm<sup>-1</sup>): 2953(m), 2907(m), 2873(m), 1444(s), 1328(m), 1323(s), 1274(w), 1239(m), 1204(w), 1096(m), 914(w), 843(s), 774(m), 695(m), 663(s), 605(m), 587(m), 577(m), 550(m), 507(m), 422(m).

Synthesis of [( $^{\rho h}$ OCO)Co(MeCN)] (3). The above representative procedure, followed by recrystallization from MeCN—toluene at -25 °C, afforded 3 as single crystals suitable for XRD in 89% yield. Anal. Calcd for C<sub>37</sub>H<sub>47</sub>CoN<sub>3</sub>O<sub>2</sub>: C, 71.14; H, 7.58; N, 6.73. Found: C, 71.41; H, 7.51; N, 6.77. ESI-MS (m/z): 655.4 [M]<sup>+</sup>. UV—vis (MeCN;  $\lambda_{max}$ , nm ( $\varepsilon$ , M<sup>-1</sup> cm<sup>-1</sup>)): 305 (19000), 427 (4900). FTIR (ATR, cm<sup>-1</sup>): 2952(m), 2903(m), 2865(m), 1476(m), 1459(m), 1427(m), 1377(m), 1356(s), 1335(m), 1301(m), 1218(m), 1199(m), 1179(w), 1158(w), 921(w), 860(s), 770(m), 737(s), 719(m), 632(m), 553(m), 436(m), 421(m).

Synthesis of [(SOCO)Co(THF)<sub>2</sub>]<sup>+</sup> (1<sup>+</sup>). A 20 mL scintillation vial was charged with 1 (607.8 mg, 1.0 mmol) and AgOTf (256.9 mg, 1.0 mmol), and these were dissolved in THF (15 mL). The resulting green suspension was stirred for 0.5 h and then filtered through a 2.0 mm pad of Celite. The solution was concentrated to ca. 5 mL, layered with pentane, and stored at -25 °C for 18 h, producing green crystals of [(SOCO)Co(THF)<sub>2</sub>][OTf] (762.6 mg, 0.92 mmol, 92% yield). Single crystals suitable for X-ray analysis were generated from the salt metathesis of [(SOCO)Co(THF)<sub>2</sub>][OTf] and Na[BPh<sub>4</sub>] in THF. Subsequent layering of pentane over the concentrated THF solution and storage at -25 °C for 18 h afforded green block X-ray-quality crystals of [(SOCO)Co(THF)2][BPh4]. Anal. Calcd for C<sub>40</sub>H<sub>60</sub>CoF<sub>3</sub>N<sub>2</sub>O<sub>7</sub>S: C, 57.96; H, 7.30; N, 3.38. Found: C, 57.77; H, 7.28; N, 3.28. UV-vis (THF;  $\lambda_{\text{max}}$ , nm ( $\varepsilon$ , M<sup>-1</sup> cm<sup>-1</sup>)): 434 (3100), 747 (2700), 878 (2000). FTIR (ATR, cm<sup>-1</sup>): 3054(m), 2953(m), 2902(m), 2865(m), 1588(m), 1556(m), 1478(m), 1440(m), 1388(m), 1359(m), 1311(m), 1241(m), 1200(m), 1124(m), 1071(m), 1026(m), 913(m), 843(m), 733(s), 700(s), 647(w), 625(m), 610(w), 580(w), 543(w), 518(w), 498(w), 471(w),

Synthesis of [(SOCO)Co(THF)<sub>3</sub>]<sup>2+</sup> (1<sup>2+</sup>). A 20 mL scintillation vial was charged with 1 (54.7 mg, 0.090 mmol) in CH<sub>2</sub>Cl<sub>2</sub> (3 mL), affording a red-orange solution. Dropwise addition of a dark blue solution of [N(p-C<sub>6</sub>H<sub>4</sub>Br)<sub>3</sub>][PF<sub>6</sub>] (118 mg, 0.188 mmol) in CH<sub>2</sub>Cl<sub>2</sub> (5 mL) gave a green-brown suspension, which was stirred for 30 min at room temperature, filtered through a pad of Celite, and washed with THF (5 mL). The filtrate was concentrated in vacuo to ca. 2 mL and layered with pentane. Standing at  $-20~^{\circ}\text{C}$  overnight deposited dark green crystals of [(SOCO)Co(THF)<sub>3</sub>][PF<sub>6</sub>]<sub>2</sub> suitable for X-ray analysis (561 mg, 0.073 mmol, 81%). The trans-disposed THF ligands can be removed under high vacuum. Because samples for elemental analysis were prepared by thorough drying in vacuo, the reported analysis is for [(SOCO)Co(THF)][PF<sub>6</sub>]<sub>2</sub>. Anal. Calcd for C<sub>35</sub>H<sub>52</sub>CoF<sub>12</sub>N<sub>2</sub>O<sub>3</sub>P<sub>2</sub>: C, 46.83; H, 5.84; N, 3.12. Found: C, 46.48; H, 6.14; N, 3.34. UV-vis (THF;  $\lambda_{\rm max}$ , nm ( $\varepsilon$ , M<sup>-1</sup> cm<sup>-1</sup>)): 436 (2700), 456 (2700), 585 (1000), 805 (1700), 874 (1600). FTIR (ATR, cm<sup>-1</sup>): 3326 (w), 2956(m), 2905(m), 2872(m), 1681(w), 1627(w), 1592(m), 1531(w), 1484(s), 1352(m), 1309(m), 1284(m), 1266(m), 1239(m), 1195(m), 1159(m), 1117(m), 1059(m), 1024(w), 1007(w), 948(w), 902(w), 818(s), 739(m), 711(w), 694(w), 650(w), 556(s), 493(s), 436(w), 416(w).

**Solid-State Magnetic Measurements.** Magnetic susceptibility data were collected using a Quantum Design MPMS XL SQUID magnetometer. All sample manipulations were performed inside a dinitrogen-filled glovebox (MBRAUN Labmaster 130). Finely ground polycrystalline samples were loaded into polyethylene bags and sealed in the glovebox, and then the bags were inserted into drinking straws and inserted into the instrument. Ferromagnetic impurities were checked through a variable field analysis (0–10 kOe) of the magnetization at 100 K; susceptibility data were collected where linearity of the *M* vs *H* plots indicated quenching of any significant

ferromagnetic impurities (Figures SM1 and SM2 in the Supporting Information). Magnetic susceptibility data were collected in the temperature range 2–300 K for 1 and 1<sup>+</sup>. Magnetization data were collected at applied fields between 0 and 50 kOe and at temperatures of 1.8 and 2 K for 1 and 1<sup>+</sup>, respectively. Data were corrected for the diamagnetic contributions of the sample holder and for the sample holding bag by subtracting empty containers; diamagnetic corrections for the samples were calculated from Pascal's constants. Magnetic susceptibility data were fit using PHI, according to the spin Hamiltonians

$$\begin{split} \hat{H} &= -2JS_1 \cdot S_2 + \sum D_i \left[ S_{z,i,1}^2 - \frac{1}{3S_{i,1}(S_{i,1} + 1)} \right. \\ &+ \left. E_i D_i (S_{x,i,1}^2 - S_{y,i,1}^2) \right] + g \mu_B \check{S}_{x,i,1} \end{split}$$

$$\hat{H} = \sum D_i \left[ S_{z,i}^2 - \frac{1}{3S_i(S_i + 1)} + E_i D_i (S_{x,i}^2 - S_{y,i}^2) \right] + g \mu_B \check{S}_{x,i}$$

**Computational Studies.** DFT geometry optimizations were performed using TURBOMOLE<sup>109</sup> coupled to the PQS Baker optimizer<sup>110,111</sup> via the BOpt package<sup>112</sup> at the BP86,<sup>113,114</sup> def2-TZVP<sup>115,116</sup> level of theory (m4 grid), on full models (including tBu groups) in the gas phase, using Grimme's version 3 (disp3, "zero damping") dispersion corrections.<sup>117</sup> All minima (no imaginary frequencies) were characterized by numerically calculating the Hessian matrix.

EPR parameters were calculated with the ADF $^{118-120}$  program system at the B3LYP/TZ2P level, using the coordinates from the structures optimized in Turbomole as input. ZORA basis sets as supplied with the ADF program were used. Unrestricted SPINORBIT ZORA COLLINEAR calculations were used to obtain the SOC corrected HFI tensors and Zeeman corrected  ${\bf g}$  tensors.

Spin density pictures were generated using IQMol (http://www.iqmol.org/).

# ASSOCIATED CONTENT

#### S Supporting Information

The Supporting Information is available free of charge on the ACS Publications website at DOI: 10.1021/acs.inorg-chem.7b01906.

Complete X-ray structure reports for [(SOCO)Co-(THF)], [(OCO)Co(MeCN)], [(SOCO)Co(MeCN)], [(PhOCO)Co(MeCN)], [(SOCO)Co(THF)<sub>2</sub>][BPh<sub>4</sub>], and [(SOCO)Co(THF)<sub>3</sub>][PF<sub>6</sub>]<sub>2</sub> and Cartesian coordinates of the DFT optimized geometries of 1–3 (PDF)

#### **Accession Codes**

CCDC 1563838–1563843 contain the supplementary crystal-lographic data for this paper. These data can be obtained free of charge via www.ccdc.cam.ac.uk/data\_request/cif, or by emailing data\_request@ccdc.cam.ac.uk, or by contacting The Cambridge Crystallographic Data Centre, 12 Union Road, Cambridge CB2 1EZ, UK; fax: +44 1223 336033.

# AUTHOR INFORMATION

# **Corresponding Authors**

\*E-mail for M.P.S.: matthew.shores@colostate.edu.

\*E-mail for B.d.B.: b.debruin@uva.nl.

\*E-mail for J.D.S.: jake.soper@gatech.edu.

#### ORCID

Caleb F. Harris: 0000-0002-6844-8923 Matthew P. Shores: 0000-0002-9751-0490 Bas de Bruin: 0000-0002-3482-7669 Jake D. Soper: 0000-0002-1961-8076

#### Notes

The authors declare no competing financial interest.

# ACKNOWLEDGMENTS

We gratefully acknowledge financial support of this work from the National Science Foundation (Grant Nos. CHE 1464852 to J.D.S. and CHE 1363274 to M.P.S.) and The Netherlands Organization for Scientific Research (NWO-CW TOP grant 716.015.001 to B.d.B.). We thank David Bostwick and Lucas Evans for mass spectrometry assistance.

#### REFERENCES

- (1) Friend, C. M.; Sanford, M. S.; Abruna, H. D. Catalytic Chemistry Workshop on Defining Critical Directions for the Future; National Science Foundation: Washington, DC, 2011.
- (2) Chirik, P. J.; Jarvo, E. R. Report on NSF SusChem Workshop and American Chemical Society Symposium; National Science Foundation: Washington, DC, 2014.
- (3) Chirik, P. J.; Wieghardt, K. Radical Ligands Confer Nobility on Base-Metal Catalysts. *Science* **2010**, 327, 794–795.
- (4) Negishi, E.-İ., Fundamental Properties of Palladium and Patterns of the Reactions of Palladium and Its Complexes. In *Handbook of Organopalladium Chemistry for Organic Synthesis*; Negishi, E.-I., de Meijere, A., Eds.; Wiley-Interscience: New York, 2002; pp 17–35.
- (5) Tasker, S. Z.; Standley, E. A.; Jamison, T. F. Recent advances in homogeneous nickel catalysis. *Nature* **2014**, *509*, 299–309.
- (6) Meijere, A. d.; Diederich, F. o. Metal-catalyzed cross-coupling reactions, 2nd ed.; Wiley-VCH: Weinheim, Germany, 2004.
- (7) Greenwood, N. N.; Earnshaw, A. Chemistry of the Elements, 2nd ed.; Butterworth Heinemann: London, 1997.
- (8) Luca, O. R.; Crabtree, R. H. Redox-active ligands in catalysis. *Chem. Soc. Rev.* **2013**, 42, 1440–1459.
- (9) Lyaskovskyy, V.; de Bruin, B. Redox Non-Innocent Ligands: Versatile New Tools to Control Catalytic Reactions. *ACS Catal.* **2012**, 2, 270–279.
- (10) Praneeth, V. K. K.; Ringenberg, M. R.; Ward, T. R. Redox-Active Ligands in Catalysis. *Angew. Chem., Int. Ed.* **2012**, *51*, 10228–10234.
- (11) Jacquet, J.; Desage-El Murr, M.; Fensterbank, L. Metal-Promoted Coupling Reactions Implying Ligand-Based Redox Changes. *ChemCatChem* **2016**, *8*, 3310–3316.
- (12) Broere, D. L. J.; Plessius, R.; van der Vlugt, J. I. New avenues for ligand-mediated processes expanding metal reactivity by the use of redox-active catechol, o-aminophenol and o-phenylenediamine ligands. *Chem. Soc. Rev.* **2015**, *44*, 6886–6915.
- (13) Haneline, M. R.; Heyduk, A. F. C-C bond-forming reductive elimination from a zirconium(IV) redox-active ligand complex. *J. Am. Chem. Soc.* **2006**, *128*, 8410.
- (14) Munha, R. F.; Zarkesh, R. A.; Heyduk, A. F. Group transfer reactions of d0 transition metal complexes: redox-active ligands provide a mechanism for expanded reactivity. *Dalton Trans.* **2013**, *42*, 3751–3766.
- (15) Zarkesh, R. A.; Ziller, J. W.; Heyduk, A. F. Four-electron oxidative formation of aryl diazenes using a tantalum redox-active ligand complex. *Angew. Chem., Int. Ed.* **2008**, 47, 4715.
- (16) Myers, T. W.; Berben, L. A. Redox active aluminium(III) complexes convert CO2 into MgCO3 or CaCO3 in a synthetic cycle using Mg or Ca metal. *Chem. Commun.* **2013**, *49*, 4175–4177.
- (17) Wong, J. L.; Sanchez, R. H.; Logan, J. G.; Zarkesh, R. A.; Ziller, J. W.; Heyduk, A. F. Disulfide reductive elimination from an iron(III) complex. *Chem. Sci.* **2013**, *4*, 1906–1910.
- (18) Bouwkamp, M. W.; Bowman, A. C.; Lobkovsky, E.; Chirik, P. J. Iron-Catalyzed [2pi + 2pi] Cycloaddition of alpha, w-Dienes: The Importance of Redox-Active Supporting Ligands. *J. Am. Chem. Soc.* **2006**, *128*, 13340–13341.
- (19) Sylvester, K. T.; Chirik, P. J. Iron-Catalyzed, Hydrogen-Mediated Reductive Cyclization of 1,6-Enynes and Diynes: Evidence

for Bis(imino)pyridine Ligand Participation. J. Am. Chem. Soc. 2009, 131, 8772–8774.

- (20) Russell, S. K.; Lobkovsky, E.; Chirik, P. J. Iron-Catalyzed Intermolecular [2 pi+2 pi] Cycloaddition. *J. Am. Chem. Soc.* **2011**, *133*, 8858–8861.
- (21) Darmon, J. M.; Stieber, S. C. E.; Sylvester, K. T.; Fernandez, I.; Lobkovsky, E.; Semproni, S. P.; Bill, E.; Wieghardt, K.; DeBeer, S.; Chirik, P. J. Oxidative addition of carbon-carbon bonds with a redoxactive bis(imino)pyridine iron complex. *J. Am. Chem. Soc.* **2012**, *134*, 17125–17137.
- (22) Jacquet, J.; Blanchard, S.; Derat, E.; Desage-El Murr, M.; Fensterbank, L. Redox-ligand sustains controlled generation of CF3 radicals by well-defined copper complex. *Chem. Sci.* **2016**, *7*, 2030–2036.
- (23) Tondreau, A. M.; Atienza, C. C. H.; Darmon, J. M.; Milsmann, C.; Hoyt, H. M.; Weller, K. J.; Nye, S. A.; Lewis, K. M.; Boyer, J.; Delis, J. G. P.; Lobkovsky, E.; Chirik, P. J. Synthesis, electronic structure, and alkene hydrosilylation activity of terpyridine and bis(imino)pyridine iron dialkyl complexes. *Organometallics* **2012**, *31*, 4886–4893.
- (24) Yu, R. P.; Darmon, J. M.; Hoyt, J. M.; Margulieux, G. W.; Turner, Z. R.; Chirik, P. J. High-activity iron catalysts for the hydrogenation of hindered, unfunctionalized alkenes. *ACS Catal.* **2012**, 2, 1760–1764.
- (25) Hojilla Atienza, C. C.; Tondreau, A. M.; Weller, K. J.; Lewis, K. M.; Cruse, R. W.; Nye, S. A.; Boyer, J. L.; Delis, J. G. P.; Chirik, P. J. High-selectivity bis(imino)pyridine iron catalysts for the hydrosilylation of 1,2,4-trivinylcyclohexane. *ACS Catal.* **2012**, *2*, 2169–2172.
- (26) Tondreau, A. M.; Atienza, C. C. H.; Weller, K. J.; Nye, S. A.; Lewis, K. M.; Delis, J. G. P.; Chirik, P. J. Iron Catalysts for Selective Anti-Markovnikov Alkene Hydrosilylation Using Tertiary Silanes. *Science* **2012**, 335, 567–570.
- (27) Villanueva, O.; Weldy, N. M.; Blakey, S. B.; MacBeth, C. E. Cobalt catalyzed sp(3) C-H amination utilizing aryl azides. *Chem. Sci.* **2015**, *6*, 6672–6675.
- (28) Bagh, B.; Broere, D. L. J.; Sinha, V.; Kuijpers, P. F.; van Leest, N. P.; de Bruin, B.; Demeshko, S.; Siegler, M. A.; Vlugt, J. I. D. Catalytic Synthesis of N-Heterocycles via Direct C(sp(3))-H Amination Using an Air-Stable Iron(III) Species with a Redox-Active Ligand. *J. Am. Chem. Soc.* **2017**, *139*, 5117–5124.
- (29) Kuijpers, P. F.; Tiekink, M. J.; Breukelaar, W. B.; Broere, D. L. J.; van Leest, N. P.; van der Vlugt, J. I.; Reek, J. N. H.; de Bruin, B. Cobalt-Porphyrin-Catalysed Intramolecular Ring-Closing C-H Amination of Aliphatic Azides: A Nitrene-Radical Approach to Saturated Heterocycles. *Chem. Eur. J.* 2017, 23, 7945–7952.
- (30) Lyaskovskyy, V.; Suarez, A. I. O.; Lu, H. J.; Jiang, H. L.; Zhang, X. P.; de Bruin, B. Mechanism of Cobalt(II) Porphyrin-Catalyzed C-H Amination with Organic Azides: Radical Nature and H-Atom Abstraction Ability of the Key Cobalt(III)-Nitrene Intermediates. *J. Am. Chem. Soc.* **2011**, 133, 12264–12273.
- (31) Olivos Suarez, A. I.; Jiang, H. L.; Zhang, X. P.; de Bruin, B. The radical mechanism of cobalt(II) porphyrin-catalyzed olefin aziridination and the importance of cooperative H-bonding. *Dalton Trans.* **2011**, 40, 5697–5705.
- (32) Das, B. G.; Chirila, A.; Tromp, M.; Reek, J. N. H.; de Bruin, B. Co-III-Carbene Radical Approach to Substituted 1H-Indenes. *J. Am. Chem. Soc.* **2016**, *138*, 8968–8975.
- (33) Paul, N. D.; Mandal, S.; Otte, M.; Cui, X.; Zhang, X. P.; de Bruin, B. Metalloradical Approach to 2H-Chromenes. *J. Am. Chem. Soc.* **2014**, *136*, 1090–1096.
- (34) Paul, N. D.; Chirila, A.; Lu, H. J.; Zhang, X. P.; de Bruin, B. Carbene Radicals in Cobalt(II)-Porphyrin-Catalysed Carbene Carbonylation Reactions; A Catalytic Approach to Ketenes. *Chem. Eur. J.* **2013**, *19*, 12953–12958.
- (35) Dzik, W. I.; Zhang, X. P.; de Bruin, B. Redox Noninnocence of Carbene Ligands: Carbene Radicals in (Catalytic) C-C Bond Formation. *Inorg. Chem.* **2011**, *50*, 9896–9903.
- (36) Dzik, W. I.; Xu, X.; Zhang, X. P.; Reek, J. N. H.; de Bruin, B. 'Carbene Radicals' in Co-II(por)-Catalyzed Olefin Cyclopropanation. *J. Am. Chem. Soc.* **2010**, *1*32, 10891–10902.

- (37) Corcos, A. R.; Villanueva, O.; Walroth, R. C.; Sharma, S. K.; Bacsa, J.; Lancaster, K. M.; MacBeth, C. E.; Berry, J. F. Oxygen Activation by Co(II) and a Redox Non-Innocent Ligand: Spectroscopic Characterization of a Radical-Co(II)-Superoxide Complex with Divergent Catalytic Reactivity. *J. Am. Chem. Soc.* **2016**, 138, 1796–1700
- (38) Hoffman, J. M.; Oliver, A. G.; Brown, S. N. The Metal or the Ligand? The Preferred Locus for Redox Changes in Oxygen Atom Transfer Reactions of Rhenium Amidodiphenoxides. *J. Am. Chem. Soc.* **2017**, *139*, 4521–4531.
- (39) Randolph, A. H.; Seewald, N. J.; Rickert, K.; Brown, S. N. Tris(3,5-di-tert-butylcatecholato)molybdenum(VI): Lewis Acidity and Nonclassical Oxygen Atom Transfer Reactions. *Inorg. Chem.* **2013**, *52*, 12587–12598.
- (40) Lippert, C. A.; Arnstein, S. A.; Sherrill, C. D.; Soper, J. D. Redox-Active Ligands Facilitate Bimetallic O2 Homolysis at Five-Coordinate Oxorhenium(V) Centers. *J. Am. Chem. Soc.* **2010**, *132*, 3879–3892.
- (41) Lippert, C. A.; Soper, J. D. Deoxygenation of Nitroxyl Radicals by Oxorhenium(V) Complexes with Redox-Active Ligands. *Inorg. Chem.* **2010**, *49*, 3682–3684.
- (42) Lippert, C. A.; Hardcastle, K. I.; Soper, J. D. Harnessing Redox-Active Ligands for Low-Barrier Radical Addition at Oxorhenium Complexes. *Inorg. Chem.* **2011**, *50*, 9864–9878.
- (43) Beletskaya, I. P.; Cheprakov, A. V. Copper in cross-coupling reactions: The post-Ullmann chemistry. *Coord. Chem. Rev.* **2004**, 248, 2337–2364.
- (44) Phapale, V. B.; Cardenas, D. J. Nickel-catalysed Negishi cross-coupling reactions: scope and mechanisms. *Chem. Soc. Rev.* **2009**, *38*, 1598–1607.
- (45) Sherry, B. D.; Fürstner, A. The Promise and Challenge of Iron-Catalyzed Cross Coupling. *Acc. Chem. Res.* **2008**, *41*, 1500–1511.
- (46) Wendlandt, A. E.; Suess, A. M.; Stahl, S. S. Copper-Catalyzed Aerobic Oxidative C-H Functionalizations: Trends and Mechanistic Insights. *Angew. Chem., Int. Ed.* **2011**, *50*, 11062–11087.
- (47) Hu, X. L. Nickel-catalyzed cross coupling of non-activated alkyl halides: a mechanistic perspective. *Chem. Sci.* **2011**, *2*, 1867–1886.
- (48) Hirano, K.; Miura, M. Copper-mediated oxidative direct C-C (hetero)aromatic cross-coupling. *Chem. Commun.* **2012**, *48*, 10704–10714.
- (49) Truong, T.; Klimovica, K.; Daugulis, O. Copper-Catalyzed, Directing Group-Assisted Fluorination of Arene and Heteroarene C-H Bonds. J. Am. Chem. Soc. 2013, 135, 9342–9345.
- (50) Yoshikai, N.; Matsumoto, A.; Norinder, J.; Nakamura, E. Iron-Catalyzed Direct Arylation of Aryl Pyridines and Imines Using Oxygen as an Oxidant. *Synlett* **2010**, *2010*, 313–316.
- (51) Sarhan, A. A. O.; Bolm, C. Iron(III) chloride in oxidative C-C coupling reactions. *Chem. Soc. Rev.* **2009**, *38*, 2730–2744.
- (52) Mako, T. L.; Byers, J. A. Recent advances in iron-catalysed cross coupling reactions and their mechanistic underpinning. *Inorg. Chem. Front.* **2016**, *3*, 766–790.
- (53) Bedford, R. B.; Brenner, P. B. The Development of Iron Catalysts for Cross-Coupling Reactions. *Top. Organomet. Chem.* **2015**, 50, 19–46.
- (54) Itazaki, M.; Nakazawa, H. Iron-Catalyzed Cross-Dehydrogenative-Coupling Reactions. *Top. Organomet. Chem.* **2015**, *50*, 47–81.
- (55) Liu, C.; Zhang, H.; Shi, W.; Lei, A. W. Bond Formations between Two Nucleophiles: Transition Metal Catalyzed Oxidative Cross-Coupling Reactions. *Chem. Rev.* **2011**, *111*, 1780–1824.
- (56) Seyferth, D. The Grignard Reagents. Organometallics 2009, 28, 1598–1605.
- (57) Tan, G.; He, S.; Huang, X.; Liao, X.; Cheng, Y.; You, J. Cobalt-Catalyzed Oxidative C-H/C-H Cross-Coupling between Two Heteroarenes. *Angew. Chem., Int. Ed.* **2016**, *55*, 10414–10418.
- (58) de Bruin, B.; Bill, E.; Bothe, E.; Weyhermuller, T.; Wieghardt, K. Molecular and electronic structures of bis(pyridine-2,6-diimine)metal complexes [ML2](PF6)(n) (n = 0, 1, 2, 3; M = Mn, Fe, Co, Ni, Cu, Zn). *Inorg. Chem.* **2000**, *39*, 2936–2947.

- (59) Budzelaar, P. H. M.; de Bruin, B.; Gal, A. W.; Wieghardt, K.; van Lenthe, J. H. Metal-to-ligand electron transfer in diiminopyridine complexes of Mn-Zn. A theoretical study. *Inorg. Chem.* **2001**, *40*, 4649–4655.
- (60) Chirik, P. J. Electronic Structures of Reduced Manganese, Iron, and Cobalt Complexes Bearing Redox-Active Bis(imino) pyridine Pincer Ligands. *Pincer and Pincer-Type Complexes: Applications in Organic Synthesis and Catalysis* **2014**, 189–212.
- (61) Smith, A. L.; Hardcastle, K. I.; Soper, J. D. Redox-Active Ligand-Mediated Oxidative Addition and Reductive Elimination at Square Planar Cobalt(III): Multielectron Reactions for Cross-Coupling. *J. Am. Chem. Soc.* **2010**, *132*, 14358–14360.
- (62) Dzik, W. I.; van der Vlugt, J. I.; Reek, J. N. H.; de Bruin, B. Ligands that Store and Release Electrons during Catalysis. *Angew. Chem., Int. Ed.* **2011**, *50*, 3356–3358.
- (63) Borré, E.; Dahm, G.; Aliprandi, A.; Mauro, M.; Dagorne, S.; Bellemin-Laponnaz, S. Tridentate Complexes of Group 10 Bearing Bis-Aryloxide N-Heterocyclic Carbene Ligands: Synthesis, Structural, Spectroscopic, and Computational Characterization. *Organometallics* **2014**, 33, 4374–4384.
- (64) Lee, M.-T.; Hu, C.-H. Density Functional Study of N-Heterocyclic and Diamino Carbene Complexes: Comparison with Phosphines. *Organometallics* **2004**, 23, 976–983.
- (65) Lummiss, J. A. M.; Higman, C. S.; Fyson, D. L.; McDonald, R.; Fogg, D. E. The divergent effects of strong NHC donation in catalysis. *Chem. Sci.* **2015**, *6*, 6739–6746.
- (66) Clavier, H.; Coutable, L.; Toupet, L.; Guillemin, J.-C.; Mauduit, M. Design and synthesis of new bidentate alkoxy-NHC ligands for enantioselective copper-catalyzed conjugate addition. *J. Organomet. Chem.* **2005**, *690*, 5237–5254.
- (67) Waltman, A. W.; Grubbs, R. H. A New Class of Chelating N-Heterocyclic Carbene Ligands and Their Complexes with Palladium. *Organometallics* **2004**, *23*, 3105–3107.
- (68) Bellemin-Laponnaz, S.; Welter, R.; Brelot, L.; Dagorne, S. Synthesis and structure of V(V) and Mn(III) NHC complexes supported by a tridentate bis-aryloxide-N-heterocyclic carbene ligand. *J. Organomet. Chem.* **2009**, *694*, 604–606.
- (69) Dagorne, S.; Bellemin-Laponnaz, S.; Romain, C. Neutral and Cationic N-Heterocyclic Carbene Zirconium and Hafnium Benzyl Complexes: Highly Regioselective Oligomerization of 1-Hexene with a Preference for Trimer Formation. *Organometallics* **2013**, *32*, 2736–2743
- (70) Romain, C.; Choua, S.; Collin, J.-P.; Heinrich, M.; Bailly, C.; Karmazin-Brelot, L.; Bellemin-Laponnaz, S.; Dagorne, S. Redox and Luminescent Properties of Robust and Air-Stable N-Heterocyclic Carbene Group 4 Metal Complexes. *Inorg. Chem.* **2014**, *53*, 7371–7376.
- (71) Romain, C.; Fliedel, C.; Bellemin-Laponnaz, S.; Dagorne, S. NHC Bis-Phenolate Aluminum Chelates: Synthesis, Structure, and Use in Lactide and Trimethylene Carbonate Polymerization. *Organometallics* **2014**, 33, 5730–5739.
- (72) Weinberg, D. R.; Hazari, N.; Labinger, J. A.; Bercaw, J. E. Iridium(I) and Iridium(III) Complexes Supported by a Diphenolate Imidazolyl-Carbene Ligand. *Organometallics* **2010**, *29*, 89–100.
- (73) Min, K. S.; Weyhermüller, T.; Bothe, E.; Wieghardt, K. Tetradentate Bis(o-iminobenzosemiquinonate(1-))  $\pi$  Radical Ligands and Their o-Aminophenolate(1-) Derivatives in Complexes of Nickel(II), Palladium(II), and Copper(II). *Inorg. Chem.* **2004**, 43, 2922–2931.
- (74) Despagnet-Ayoub, E.; Henling, L. M.; Labinger, J. A.; Bercaw, J. E. Addition of a phosphine ligand switches an N-heterocyclic carbene-zirconium catalyst from oligomerization to polymerization of 1-hexene. *Dalton Trans.* **2013**, *42*, 15544–15547.
- (75) Chaudhuri, P.; Wieghardt, K. Phenoxyl Radical Complexes. In Progress in Inorganic Chemistry. *John Wiley & Sons, Inc* **2002**, 151–216
- (76) Gurley, L.; Beloukhina, N.; Boudreau, K.; Klegeris, A.; McNeil, W. S. The synthesis and characterization of a series of cobalt(II) beta-

ketoaminato complexes and their cytotoxic activity towards human tumor cell lines. *J. Inorg. Biochem.* **2011**, *105*, 858–866.

- (77) Chiang, L.; Allan, L. E. N.; Alcantara, J.; Wang, M. C. P.; Storr, T.; Shaver, M. P. Tuning ligand electronics and peripheral substitution on cobalt salen complexes: structure and polymerisation activity. *Dalton Trans.* **2014**, *43*, 4295–4304.
- (78) Nguyen, A. I.; Hadt, R. G.; Solomon, E. I.; Tilley, T. D. Efficient C-H bond activations via O-2 cleavage by a dianionic cobalt(II) complex. *Chem. Sci.* **2014**, *5*, 2874–2878.
- (79) Kochem, A.; Kanso, H.; Baptiste, B.; Arora, H.; Philouze, C.; Jarjayes, O.; Vezin, H.; Luneau, D.; Orio, M.; Thomas, F. Ligand Contributions to the Electronic Structures of the Oxidized Cobalt(II) salen Complexes. *Inorg. Chem.* **2012**, *51*, 10557–10571.
- (80) Meng, Y.-S.; Mo, Z.; Wang, B.-W.; Zhang, Y.-Q.; Deng, L.; Gao, S. Observation of the single-ion magnet behavior of d8 ions on two-coordinate Co(i)-NHC complexes. *Chem. Sci.* **2015**, *6*, 7156–7162.
- (81) Massard, A.; Braunstein, P.; Danopoulos, A. A.; Choua, S.; Rabu, P. Studies on Three-Coordinate  $[Co\{N(SiMe3)2\}2L]$  Complexes, L = N-Heterocyclic Carbene. *Organometallics* **2015**, 34, 2429–2438.
- (82) Harrison, D. J.; Daniels, A. L.; Korobkov, I.; Baker, R. T. Tetracarbonyl(trifluoromethyl)cobalt(I) [Co(CO)4(CF3)] as a Precursor to New Cobalt Trifluoromethyl and Difluorocarbene Complexes. *Organometallics* **2015**, *34*, 4598–4604.
- (83) Danopoulos, A. A.; Braunstein, P. Mono-N-heterocyclic carbene amido and alkyl complexes. Cobalt-mediated C-H activation and C-C coupling reactions involving benzyl ligands on a putative 3-coordinate intermediate. *Dalton Trans.* **2013**, *42*, 7276–7280.
- (84) Gibson, S. E.; Johnstone, C.; Loch, J. A.; Steed, J. W.; Stevenazzi, A. Novel Structures and Pauson–Khand Activities of N-Heterocyclic Carbene Dicobalt Complexes. *Organometallics* **2003**, 22, 5374–5377.
- (85) Coleman, A. W.; Hitchcock, P. B.; Lappert, M. F.; Maskell, R. K.; Müller, J. H. Routes to optically active electron-rich olefins (L\*2 and some derived carbenemetal complexes; x-ray structures of [Co(CO)(L\*)(NO(PPh3)] and cis-[Rh(Cl)(COD)(L\*\*)][L\*= (S)-CN(Me)CH(Me)CH2NMe. J. Organomet. Chem. 1983, 250, c9—c14.
- (86) Liske, A.; Verlinden, K.; Buhl, H.; Schaper, K.; Ganter, C. Determining the pi-Acceptor Properties of N-Heterocyclic Carbenes by Measuring the Se-77 NMR Chemical Shifts of Their Selenium Adducts. *Organometallics* **2013**, 32, 5269–5272.
- (87) Miessler, G. L.; Tarr, D. A. *Inoganic Chemistry*, 2nd ed.; Prentice Hall: Englewood Cliffs, NJ, 1998.
- (88) Lagaditis, P. O.; Schluschass, B.; Demeshko, S.; Wurtele, C.; Schneider, S. Square-Planar Cobalt(III) Pincer Complex. *Inorg. Chem.* **2016**, 55, 4529–4536.
- (89) Addison, A. W.; Rao, T. N.; Reedijk, J.; van Rijn, J.; Verschoor, G. C. Synthesis, structure, and spectroscopic properties of copper(II) compounds containing nitrogen-sulphur donor ligands; the crystal and molecular structure of aqua[1,7-bis(N-methylbenzimidazol-2[prime or minute]-yl)-2,6-dithiaheptane]copper(II) perchlorate. *J. Chem. Soc., Dalton Trans.* 1984, 1349–1356.
- (90) Chilton, N. F.; Anderson, R. P.; Turner, L. D.; Soncini, A.; Murray, K. S. PHI: A powerful new program for the analysis of anisotropic monomeric and exchange-coupled polynuclear d- and f-block complexes. *J. Comput. Chem.* **2013**, *34*, 1164–1175.
- (91) Cole, G. M.; Garrett, B. B. Atomic and Molecular Spin-Orbit Coupling Constants for 3d Transition Metal Ions. *Inorg. Chem.* **1970**, 9, 1898.
- (92) Jenkins, D. M.; Di Bilio, A. J.; Allen, M. J.; Betley, T. A.; Peters, J. C. Elucidation of a low spin cobalt(II) system in a distorted tetrahedral geometry. *J. Am. Chem. Soc.* **2002**, *124*, 15336–15350.
- (93) Shores, M. P.; Sokol, J. J.; Long, J. R. Nickel(II)-molybdenum-(III)-cyanide clusters: Synthesis and magnetic behavior of species incorporating [(Me<sub>3</sub>tacn)Mo(CN)<sub>3</sub>]. *J. Am. Chem. Soc.* **2002**, *124*, 2279–2292.
- (94) Radonovich, L. J.; Klabunde, K. J.; Behrens, C. B.; McCollor, D. P.; Anderson, B. B. Crystal and molecular structures of  $\pi$ -toluene complexes of bis(pentafluorobenzene)cobalt and bis-(pentafluorobenzene)nickel. *Inorg. Chem.* 1980, 19, 1221–1226.

- (95) Chaudhuri, P.; Verani, C. N.; Bill, E.; Bothe, E.; Weyhermüller, T.; Wieghardt, K. Electronic Structure of Bis(o-iminobenzosemiquinonato)metal Complexes (Cu, Ni, Pd). The Art of Establishing Physical Oxidation States in Transition-Metal Complexes Containing Radical Ligands. J. Am. Chem. Soc. 2001, 123, 2213–2223.
- (96) Urbach, F. L.; Bereman, R. D.; Topich, J. A.; Harihara, M.; Kalbache, Bj. Stereochemistry and Electronic-Structure of Low-Spin, Square-Planar Cobalt(II) Chelates with Tetradentate Schiff-Base Ligands. J. Am. Chem. Soc. 1974, 96, 5063—5069.
- (97) Dong, W. K.; Duan, J. G.; Guan, Y. H.; Shi, J. Y.; Zhao, C. Y. Synthesis, crystal structure and spectroscopic behaviors of Co(II) and Cu(II) complexes with Salen-type bisoxime ligands. *Inorg. Chim. Acta* **2009**, 362, 1129–1134.
- (98) Cantalupo, S. A.; Fiedler, S. R.; Shores, M. P.; Rheingold, A. L.; Doerrer, L. H. High-Spin Square-Planar Co<sup>II</sup> and Fe<sup>II</sup> Complexes and Reasons for Their Electronic Structure. *Angew. Chem., Int. Ed.* **2012**, *51*, 1000–1005.
- (99) Chirik, P. J. Preface: Forum on Redox-Active Ligands. *Inorg. Chem.* 2011, 50, 9737–9740.
- (100) Morris, W. D.; Wolczanski, P. T.; Sutter, J.; Meyer, K.; Cundari, T. R.; Lobkovsky, E. B. Iron and Chromium Complexes Containing Tridentate Chelates Based on Nacnac and Imino- and Methyl-Pyridine Components: Triggering C-X Bond Formation. *Inorg. Chem.* 2014, 53, 7467–7484.
- (101) Williams, V. A.; Wolczanski, P. T.; Sutter, J.; Meyer, K.; Lobkovsky, E. B.; Cundari, T. R. Iron Complexes Derived from {nacnac-(CH(2)py)(2)}(-) and {nacnac-(CH(2)py)(CHpy)}(n) Ligands: Stabilization of Iron(II) via Redox Noninnocence. *Inorg. Chem.* **2014**, *53*, 4459–4474.
- (102) Boehme, C.; Frenking, G. Electronic structure of stable carbenes, silylenes, and germylenes. J. Am. Chem. Soc. 1996, 118, 2039–2046.
- (103) Herrmann, W. A. N-heterocyclic carbenes: A new concept in organometallic catalysis. *Angew. Chem., Int. Ed.* **2002**, *41*, 1290–1309.
- (104) Fulmer, G. R.; Miller, A. J. M.; Sherden, N. H.; Gottlieb, H. E.; Nudelman, A.; Stoltz, B. M.; Bercaw, J. E.; Goldberg, K. I. NMR Chemical Shifts of Trace Impurities: Common Laboratory Solvents, Organics, and Gases in Deuterated Solvents Relevant to the Organometallic Chemist. *Organometallics* 2010, 29, 2176–2179.
- (105) Evans, D. F. The Determination of the Paramagnetic Susceptibility of Substances in Solution by Nuclear Magnetic Resonance. *J. Chem. Soc.* **1959**, 2003–2005.
- (106) Piguet, C. Paramagnetic susceptibility by NMR: The 'solvent correction' removed for large paramagnetic molecules. *J. Chem. Educ.* **1997**, 74, 815–816.
- (107) Rhile, I. J.; Markle, T. F.; Nagao, H.; DiPasquale, A. G.; Lam, O. P.; Lockwood, M. A.; Rotter, K.; Mayer, J. M. Concerted Proton—Electron Transfer in the Oxidation of Hydrogen-Bonded Phenols. *J. Am. Chem. Soc.* **2006**, *128*, 6075–6088.
- (108) Bain, G. A.; Berry, J. F. Diamagnetic corrections and Pascal's constants. J. Chem. Educ. 2008, 85, 532-536.
- (109) TURBOMOLE Version 7.1; TURBOMOLE Gmbh, Karlsruhe, Germany, 2013.
- (110) PQS Version 2.4; Parallel Quantum Solutions, Fayetteville, AR, USA 2001
- (111) Baker, J. An Algorithm for the Location of Transition-States. *J. Comput. Chem.* **1986**, *7*, 385–395.
- (112) Budzelaar, P. H. M. Geometry optimization using generalized, chemically meaningful constraints. *J. Comput. Chem.* **200**7, 28, 2226–2236.
- (113) Becke, A. D. Density-Functional Exchange-Energy Approximation with Correct Asymptotic-Behavior. *Phys. Rev. A: At., Mol., Opt. Phys.* **1988**, *38*, 3098–3100.
- (114) Perdew, J. P. Density-Functional Approximation for the Correlation-Energy of the Inhomogeneous Electron-Gas. *Phys. Rev. B: Condens. Matter Mater. Phys.* **1986**, 33, 8822–8824.
- (115) Weigend, F.; Ahlrichs, R. Balanced basis sets of split valence, triple zeta valence and quadruple zeta valence quality for H to Rn:

Design and assessment of accuracy. *Phys. Chem. Chem. Phys.* **2005**, *7*, 3297–3305.

- (116) Weigend, F.; Haser, M.; Patzelt, H.; Ahlrichs, R. RI-MP2: optimized auxiliary basis sets and demonstration of efficiency. *Chem. Phys. Lett.* **1998**, 294, 143–152.
- (117) Grimme, S.; Antony, J.; Ehrlich, S.; Krieg, H. A consistent and accurate ab initio parametrization of density functional dispersion correction (DFT-D) for the 94 elements H-Pu. *J. Chem. Phys.* **2010**, 132, 154104.
- (118) Baerends, E. J.; Ellis, D. E.; Ros, P. Self-consistent molecular Hartree-Fock-Slater calculations I. The computational procedure. *Chem. Phys.* **1973**, *2*, 41–51.
- (119) te Velde, G.; Baerends, E. J. Numerical-Integration for Polyatomic Systems. *J. Comput. Phys.* **1992**, *99*, 84–98.
- (120) Fonseca Guerra, C.; Snijders, J. G.; te Velde, G.; Baerends, E. J. Towards an order-N DFT method. *Theor. Chem. Acc.* **1998**, *99*, 391–403.